Multisensory Wearable Motion Analysis in Spine Biomechanics

Tesi di Dottorato

Dottorato di Ricerca in:
Automatica, Robotica e Bioingegneria
Ciclo XX (2005)

Supervisore: Prof. Danilo De Rossi
Chiar.mo Prof. Andrea Caiti
Studente:
Raphaël Bartalesi

Università degli Studi di Pisa
Dipartimento di Sistemi Elettrici e Automazione

Contents

List of Figures

List of Tables

Chapter 1

Introductory concepts of anatomy, biomechanics and pathology of the lumbar spine

1.1 Low Back Disorders: a contemporary problem

In the contemporary society, low back disorders (LBD) are inducing physicians and biomechanists to a deep study of the complex and interconnecting factors that are responsible of a socioeconomical disease.

The understanding of the biochemical and biomechanical properties of the vertebra, disc and ligaments has been broadened by more refined research methods. Many disciplines including bioengineering, basic science research, medicine and epidemiology are now involved in the analysis of lumbar disorders and low back pain (LBP) ([1]).

Studies suggest that between 60% and 90% of people will suffer from low back disorders at some point in their life and that at any one time between 15% and 42% of people are suffering (depending on the study population and the definition of back pain used). Data from the European survey on working conditions ([2]) reveal that 30% of European workers suffer from back pain, which tops the list of all reported work-related disorders. Although in most cases patients make a full recovery from an episode of low back pain (60-70% recover within 6 weeks, 70-90% within 12 weeks) this still adds up to a very large amount of lost time from work. In addition the recurrence rate for low back disorders is very high. Although precise figures do not exist, estimates from Member States of the economic costs of all work related ill health range from 2.6 to 3.8% of Gross National Product.

1.2 Origin of Low Back Disorders

The exact origin (or etiology) of LBD are often not clear. Current knowledge cannot always determine the exact medical cause of low back pain by clinical examination or laboratory tests. While there is sometimes a relationship between pain and findings on magnetic resonance imaging of disc abnormalities (such as with a herniated disc or clinical findings on nerve compression), the most common form of back disorders is non-specific symptoms ([3]). On average 95%

of LBD are called non-specific or strain/sprain because the source of the pain is unknown. Furthermore, the pain may arise from any of the spinal structures - disc, facets, ligaments, vertebrae, tendons and muscles and a differentiation between the multiple causes is often impossible. So, conventionally, the origins of low back pain are grouped under four categories:

- discogenic/neurological;
- muscular/ligamentous;
- structural;
- other disorders.

, Since the exact origin or etiology of the disorder is often not evident and the effect of prevention is not always positive, more research into LBD is necessary, both in laboratory studies to reveal more scientific background but also in the working environment itself to quantify specific risks.

1.3 Physiological Function of the Spine

In the muskoloskeletal system, the spine holds the difficult task of ensuring the stability of the trunk and supports the upper extremity girdles and the pelvic girdle ([4]). At times, these functions are altered and compromised as a result of degenerative, traumatic, neoplastic and other patologies that lead to LBD.

The efficiency and equilibrium in the distribution of work loads, in both antigravity statics and mobility, are determined by the coordination of the various segments comprising the spine, i.e. the *functional units*, referring to the complex of two adjacent vertebrae and the interposed intervertebral disc. The functional units are stacked between them and comprise the spine articular complex (see Figs. 1.1(a) and 1.1(b)).

1.4 Biomechanics of the spine

The lumbar spine is an element of transmission and adaptation that, like an elastic shock absorber, feels the impact of any overlying and underlying disequilibrium.

The role of the intervertebral disc (Fig. 1.2), cornerstone of spinal statics, is to absorb shocks and transmit the load through the vertebral bodies as well as to allow movements of the adjacent functional units. It is composed of three parts: a nucleus polposus, a highly hydrated central gelatinous mass, the fibrous ring (or annulus fibrosus), a circular fibrous part which surrounds and contains the nucleus polposus, and the superficial portion of the vertebral plate, made of a cartilagenous layer which covers the upper and lower surfaces of the intervertebral disc.

Together with the position of the spine in space, the lumbar lordosis affects the amount of intradiscal pressure, which is higher when sitting (particularly with flexed trunk) than when standing, as shown by [5]. Intra-abdominal pressure (IAP) also plays an important role in spinal statics and in the prevention of LBD.

The layout of the lumbar spine affects the weight distribution between the anterior and the posterior portions of the disc: greater anterior load with reduced lordosis, greater posterior compression

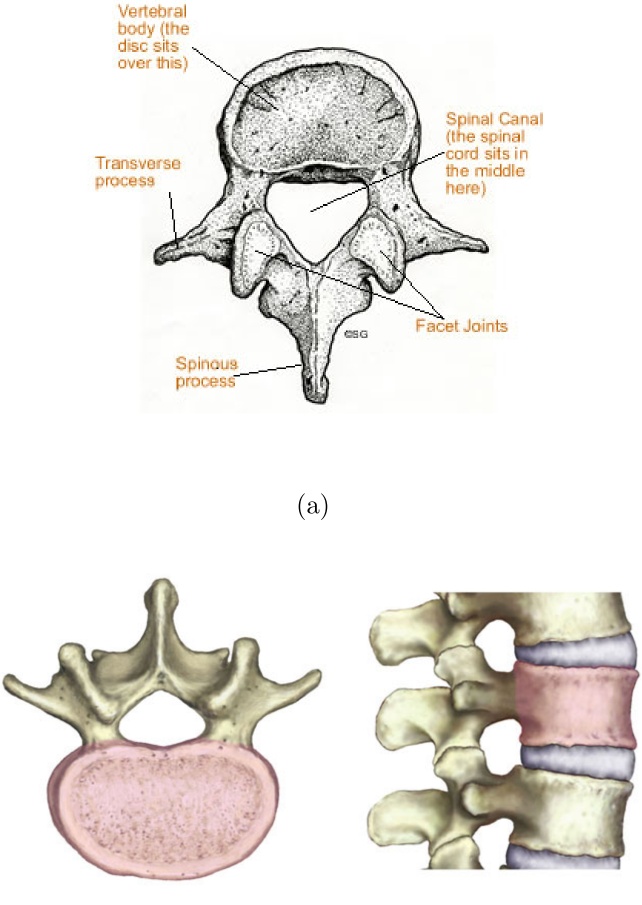

(a)

(b)

Figure 1.1: (a) Nomenclature of the spine vertebral body - (b) Upper and lateral view of the vertebral body.

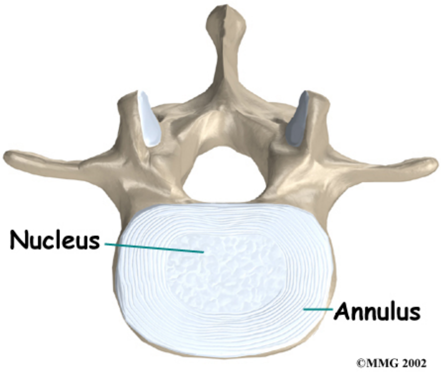

Figure 1.2: The intervertebral disc: distinction between annulus fibrosus and nucleus polposus.

with increased lordosis.

Statically, the presence of curves in the spine increases the resistance to axial compression stresses. Lumbar lordosis in thus essential to reduce load on intevertebral discs (Fig. 1.3), maintaining the nucleus gel in a more anterior position and to prevent its posterior protrusion. The maintainance of the lumbar curvature, IAP and tone of the paravertebral muscles actually strengthen the spine and are essential in the prevention of injuries when lifting weights. Lumbar lordosis is thus an important element in both static and dynamic physiology. An increase, a reduction or altered distribution of this spinal curve inevitably changes the functionality of the spine and can promote the occurrence of subsequential mechanical stress, mostly at the disc level, leading in what is generally called *disc degeneration*.

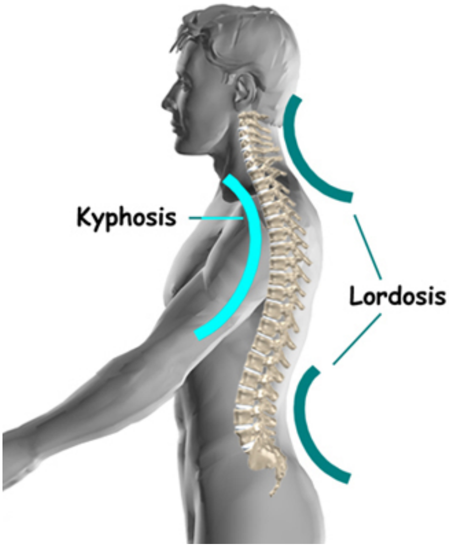

Figure 1.3: The spinal functional curves in the sagittal balance.

1.5 Disc degeneration

Disc degeneration can occur at any age, but is much more common in older discs. Degeneration is associated with gross structural changes which affect the annulus and endplate of lower lumbar discs (Fig. 1.4), including circumferential and radial tears in annulus, increased radial bulging of the outer annulus, inwards buckling of the inner annulus, reduced disc height, endplate defects and vertical bulging of the endplates into the adjacent vertebral bodies ([1]).

Structural failure is permanent, because of the low metabolic rate of adult disc renders them incapable of repairing gross defects. Furthermore, structural failure naturally progresses, by physical and biological mechanisms, and so is a suitable marker for a degenerative process that is likely spreading as crack propagation occurs in engineering materials.

Biological mechanisms of progression depend on the fact that a healthy disc tends to equalise pressure within it, whereas a disrupted disc exhibits high concentrations of compressive stress in the annulus, and a decompressed nucleus. Reduced nucleus pressure impairs proteoglycan synthesis, so the aggrecan and water content of a decompressed nucleus would progressivley fall. This is the opposite of what is required to restore normal disc function.

Structural damages of discs can be created by injury or by wear-and-tear fatigue loading. Although mechanical disruption can precipitate degeneration, the most important cause of human disc degeneration could be the various process which weaken a disc prior to disruption, or which impair its healing response. The combined effects of an unfavourable inheritance, middle age, inadequate metabolite transport and loading history, appear to weaken discs to such an extent that physical disruption follows some minor incidents.

1.6 Spinal instability

There is some relationship between engineering and spinal instability. It must be distinguished between major disorders, like spondilolysis or scolyosis and degenerative instability: this last one refers to back pain exacerbated by movement and associated with intersegmental movements that are abnormal or excessive at one or more levels. The biomechanical evidence suggests that segmental instability is best defined in terms of reduced resistance to movement ([1]), leading

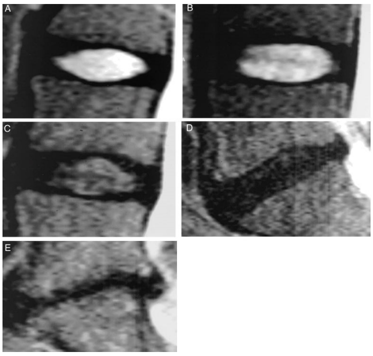

Figure 1.4: Grading system for the assessment of lumbar disc degeneration ([6]): *Grade I*: the structure of the disc is homogeneous, with bright hyperintense white signal intensity any normal disc height. *Grade II*: the structure of the disc is inhomogeneous, with the hyperintense white signal. The distinction between nucleus and annulus is clear, and the disc height is normal, with or without a horizontal gray bands. *Grade III*: the structure of the disc is inhomogeneous, with an intermittent gray signal intensity. The distinction between nucleus and annulus is unclear, and the disc height is normal or slightly decreased. *Grade IV*: the structure of the disc is inhomogeneous, with a hypointense dark gray signal intensity. The distinction between the nucleus and annulus is lost, the disc height is normal or moderately decreased. *Grade V*: the structure of the disc is inhomogeneous, with a hypointense black signal intensity. The distinction between nucleus and annulus is lost, and the disc space is collapsed. Grading is performed on T2-weighted Mid-sagittal fast spin-echo images.

to defining it as a condition in which a motion segment exhibits an abnormal magnitude or direction of movement when subjected to a normal load.

Intervertebral discs provide most of the spine's intrinsic resistance to small movements and disc degeneration is widely associated withe segmental instability. Injuries to the supraspinous ligament are also a common cause of spinal instability. A disc that is narrowed or decompressed will also produce a lack of tension in the ligaments, leading to instability as well.

Chapter 2

Determination of lumbar spine posture

2.1 The sagittal balance

The large diffusion of LBD (Sec. 1.1) has induced a deep research on their causes: many factors are contributing on lumbar disorders and frequently they are interconnected, but most are linked to working conditions and to improper postural habits ([7]).

It is widely agreed that in clinical evaluation there is the need of a device able to monitorize the lumbar spine posture and gesture directly in the field during normal daily activities. Furthermore there is the need of a relation between external epithelial measurements and the internal configuration of spine functional units, that is normally availaible with other measurement systems, such as MRI and X-rays.

Spinal posture can be charaterized in various ways, depending on the shape or curvature of the spinal column and the orientation of the entire column in respect to a reference frame. Actually, spine is continuosly subjected to compressive forces required to balance the external moments genrated by gravity and other weights acting on the trunk and on lower limbs; spinal loading is minimized when the vertebral column is balanced vertically on the pelvis or when it is supported by the back on a chair or on a flat surface. Quite separate from the effect of trunk inclination and the presence of curvature is the effect of spine curvature itself ([1]).

The sagittal balance is fundamental in spinal posture analysis because it is in this plane that curvatures lie. It is useful and common to define spinal posture in terms of the angle subtended between the upper surface of L1 vertebral body and the top of the sacrum S1 (Fig. 2.2(a)). This angle is commonly and not properly defined as lumbar curvature, or lumbar lordosys.

2.2 Lumbar spine monitorization with external measurement systems

The precise amount of lumbar flexion or extension in a given posture can be quantified from changes in lumbar curvature, and this value can be measured from stereophotogrammetry (commonly X-rays and NMR), but it can also be estimated by measuring the angle between the tangents to the surface of the back at L1 and S2. In those locations the skin is approximately orthogonal to the top surfaces of vertebral bodies. Although skin movements can lead to small differences, expecially in lordotic postures, changes in lumbar curvature

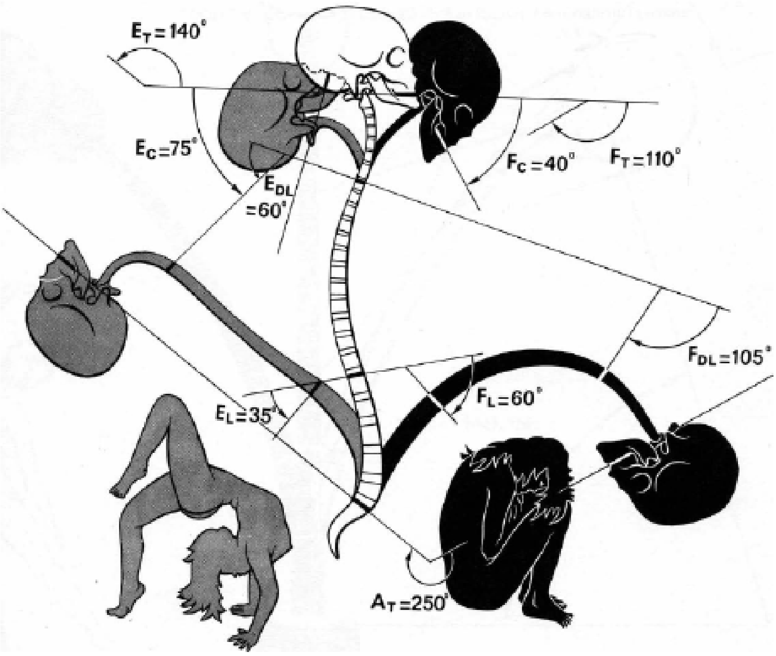

Figure 2.1: Physiological flexion/extension ROM of spine. Source: [8]

should correspond precisely to changes measured at skin surfaces. Fig. 2.2(b) shows the ISOTRACK device designed for quantifying lumbar curvature from external measurements.

Furthermore, in the last decade, many efforts were made in order to assess spine curvatures with external measurement methods, considering them a fundamental instrument at every step of the clinical history of a patient: a wide classification of these methods is

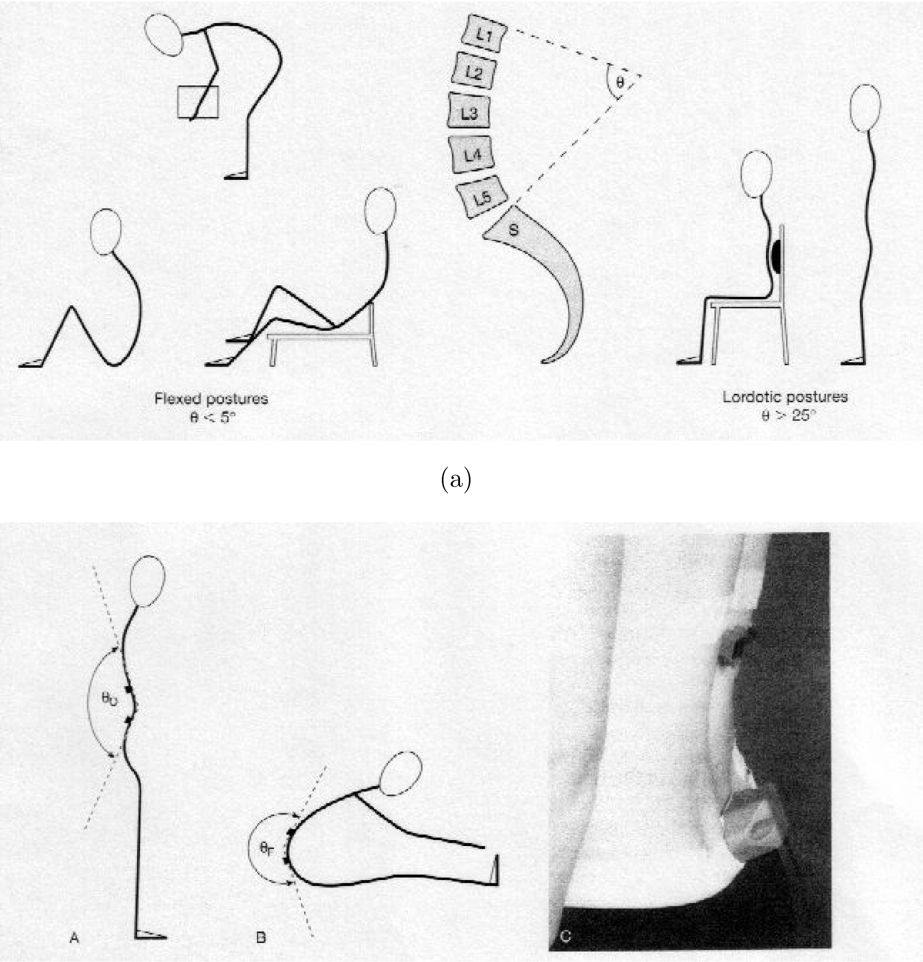

(a)

(b)

Figure 2.2: (a) Definition of flexed and lordotic posture in terms of the lumbar angle θ. Typical values for cadaveric and unloaded spine are comprised between 41-45°, whereas in vivo standing and unsupported sitting are respectively comprised between 49-61° and 22-34°. (b) The ISOTRACK device, using inclinometers to measure lumbar curvature. Source: [1]

Figure 2.3: BACES system developed by at Centro di Riabilitazione Infantile di Udine, Italy.

availaible in [9]. Figures 2.3, 2.4, 2.5 and 2.6 show some of these devices developed in order to assess spine geometry, but actually none of them combine the features of being non-invasive, unobtrusive and comfortable in order to be used in long-term and in-field analysis.

2.3 Relation between external measurements and vertebrae ROM

Recent studies compared data obtained by inclinometers and other external devices with geometrical parameters of lumbar vertebraes[1] obtained by stereophotogrammetry (Fig. 2.7). The obtained accuracy of linear regressions is very encouraging, because correlation coefficients are often greater than 0.9 ([10]). Furthermore, the prediction accuracy is better in flexion than in extension ([11]).

---

[1] Such as the angle between subsequent endplates in the sagittal plane.

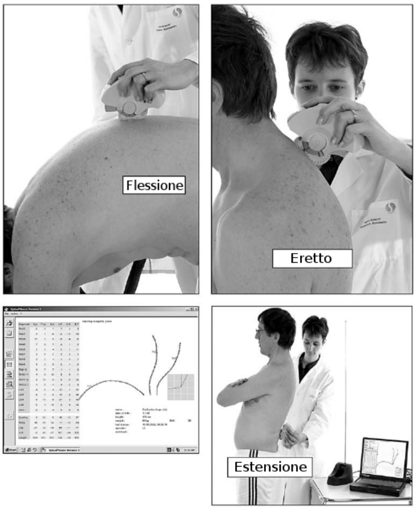

Figure 2.4: Measures of spinal curves with the *Spinal Mouse* (Aditus Systems, USA) in different position and typical output of a series of test.

Figure 2.5: The Lumbar Motion Monitor system (LMM, Chattecx Corp. USA).

Figure 2.6: Use of Inertial Measuring Units (IMU) in posture reconstruction (CBIM-UNIPI, Italy).

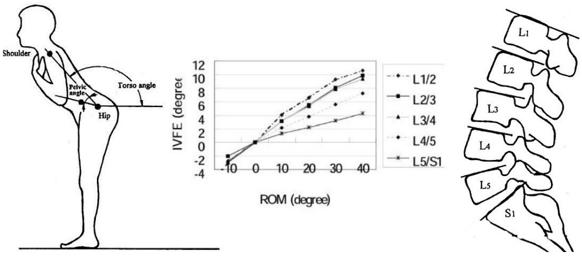

Figure 2.7: Correlation between external measures and vertebrae ROM.

These data are so suitable to be used in biomechanical analysis in order to predict forces and moments acting on the functional units of the lumbar spine.

Chapter 3

Multisensory wearable motion analysis of lumbar spine

3.1 Introduction

In this study we developed a wearable garment for the monitorization of the lumbar curvature and its relation with posture adopting a multisensory hybrid approach. The system has been developed using piezoresistive conductive-elastomer and integrated MEMS accelerometers (Sec. 3.2.1 and 3.2.3). Furthermore it has been designed in order to match smart clothes requirements, resulting:

- comfortable;
- unobtrusive;
- low-cost.

Figure 3.1: The sensorized prototype realized on a rowing Lycra suite.

As shown in figure 3.1 a single strip of elastomer was spread onto a rowing Lycra suite. This suite resulted very adherent to the body during all tasks, except in the final part of hyperextensions in the sagittal plane where some creases could occur.

An ad-hoc acquisition device has been developed for the current prototype and data has been transmitted by wired cables and processed using the *Matlab Simulink* toolbox. A special garment[1] has been developed for the Biomedical Informatics Laboratory of the University of Pavia (Italy) using the *SEW* Bluetooth data transmission device developed by the electronic swiss factory CSEM.

---

[1] Not shown in this report.

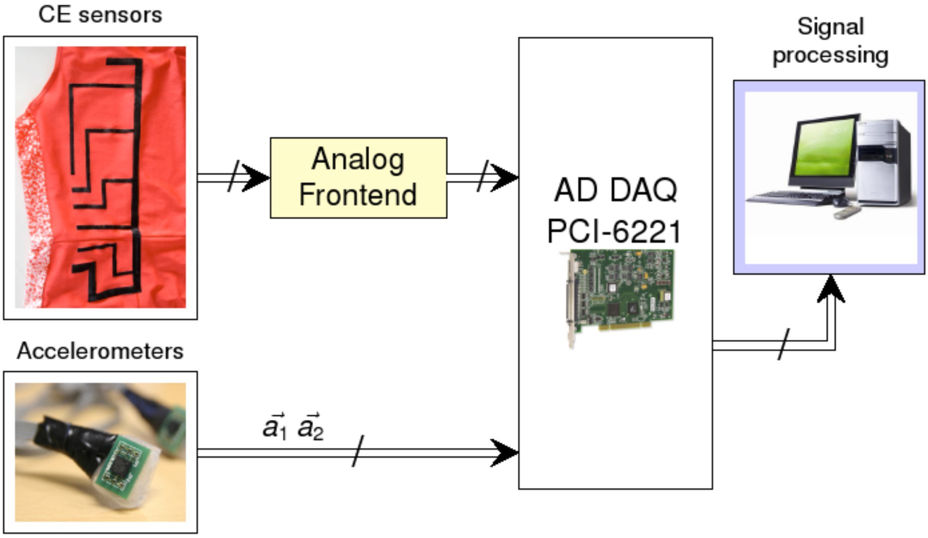

Figure 3.2: The multisensory model.

As explained in Sec. 3.2.1 and 3.2.3, processing CEs signals and accelerometers signals separately (although in a redundant way) is not suitable for describing completely the behaviour of the system, but a fusion of information is the way to mutually overcome their respective limitations: accelerometers do not provide information about deformations and the non-linearities of CEs avoid their use in inverse-dynamics applications ([12]). The fusion of redundant data coming from different sensors in a single model is commonly called a *multisensory data model* (Fig. 3.2). This technique is widely used in data processing and in navigation applications, where complementary Kalman filtering often provides very good prediction results ([13]).

The system has been calibrated with a dedicated hardware and trials has been performed with an external stereophotogrammetric system as reference (Sec. 3.3).

The concept resulted robust, providing furthermore the way to overcome the single technology limitations and to crosscheck error scenarios. This technique will open the possibility of long-term monitoring of posture and gesture of lumbar spine and other body segments, finding its proper application in ergonomy and in computational biomechanics.

3.2 Sensors and methods

3.2.1 Electrically conductive elastomers

Experimental trials proved that during flexion and extension tasks the epithelium deformation in the lumbar skin is very high, up to 60% in respect to a neutral upstanding posture. With such range of elongation, Electrically Conductive Elastomer composites (CEs) are a good fit for measuring deformations.

CEs show piezoresistive properties when a deformation is applied. They can be integrated into fabric or into other flexible substrate and employed as strain gauge sensors (Fig. 3.3). CE we used is a commercial product by WACKER Ltd (Elastosil LR 3162 A/B) and it consists of a mixture containing graphite and silicone rubber. WACKER Ltd guarantees the non-toxicity of the product that, after vulcanisation, can be employed in medical and pharmaceutical applications. Further information on mathematical modelling of these sensors is reported on Sec. 4.2, while electronic front-end and signal

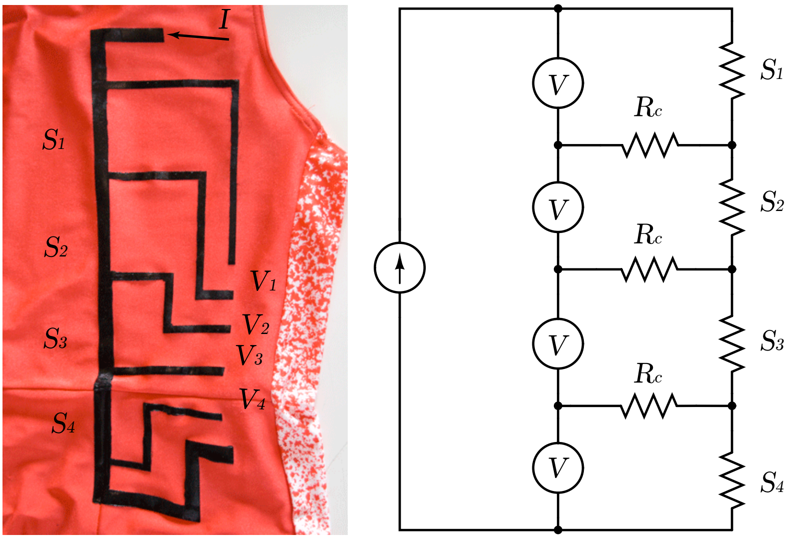

Figure 3.3: Smeared strip of conductive elastomer on the lumbar part of the Lycra rowing suite with indications of sensors (S_i) and relative electrical model.

processing of CEs is described in [12].

3.2.2 CEs hybrid model identification

The non-linear behaviour of CEs places a limitation for their use in inverse-dynamics tasks: reading the real-time electrical value is insufficient to determine the mechanical deformation that caused a change in resistance. Furthermore, the relaxation time is too long to suitably code human movements ([12]).

Due to the aforementioned reasons, CEs has been modeled considering a different behaviour in elongation and in relaxation: actually, when the sensor in stretched, the internal cross-links of the

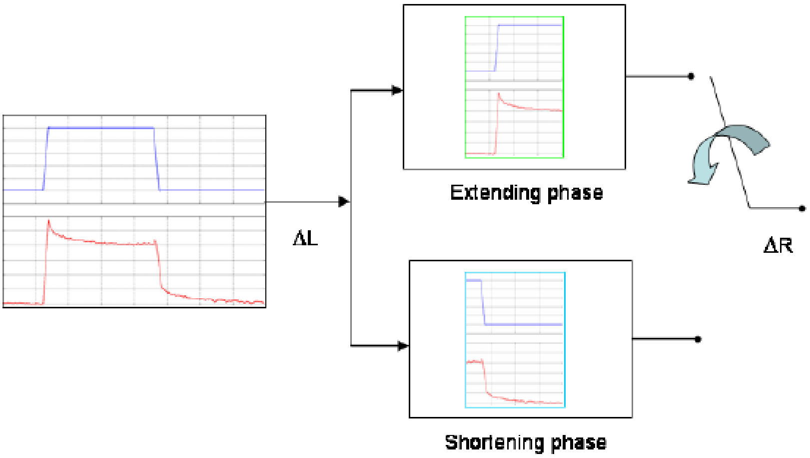

Figure 3.4: The blackbox hybrid model. In the left the red line corresponds to the CE resistance, that is the electrical response to a trapezoidal ramp in mechanical deformation (blue line). In the right, the CE output is separated in two distinct phases corresponding to elongation and relaxation. A switch in then needed to control which function has to be employed.

polymeric chains tend to break. Inversely, when the sensor is relaxed, the cross-link readjustment lead to different electrically conductive paths in respect to the previous states. The mathematical models of CEs used in this work have been developed in [14] using a blackbox system identification approach (Fig. 3.4).

It is clear that the decision of which model has to be used during data processing must be assessed by an external switch control that

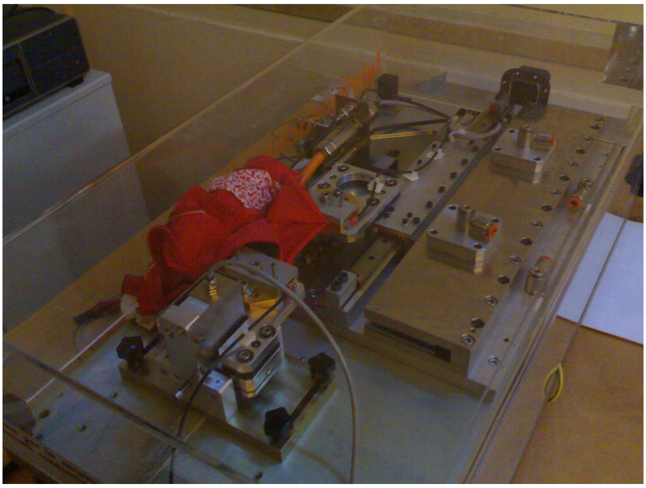

Figure 3.5: The calibration hardware used for system identification. Courtesy of *Smartex* laboratories, Navacchio (PI), Italy.

knows if the CE sensor is in the elongation phase or in the relaxation phase. This task is performed by accelerometers and is described in Sec. 3.2.4.

In order to estimate both subsystems, a dedicated calibration hardware has been used (Fig. 3.5), while the ARMAX[2] model has been chosen in the *Matlab System Identification Toolbox*.

1. *Elongation.* During this phase the system behaviour is quite similar to a second order LCTI system (with characteristic overshoot and exponential relaxation). The transfer function relating the electrical resistance output $Y_1(s)$ to the mechanical

---

[2] ARMAX stands for linear parametrical autoregressive system with moving average noise filtering and extra output.

deformation $U_1(s)$ can be written as:

$$G_1(S) = \frac{Y(S)}{U(S)} = A_1 \frac{\left(1 + \frac{S}{z_1}\right)\left(1 + \frac{S}{z_2}\right)}{\left(1 + \frac{2\xi}{\omega}S + \frac{S^2}{\omega}\right)\left(1 + \frac{S}{p_1}\right)} \tag{3.1}$$

Due to the improper ratio of polynomial degrees in $G_1(s)$, a high frequency pole at 100MHz has been added without influencing the band of interest. The estimated coefficients for eq. 3.1, extracted are reported in table 3.1:

Table 3.1: Coefficients for $G_1(S)$.

A_1	z_1	z_2	$1/\omega$	$2\xi/\omega$	p_1
801	0.6762	0.0768	0.258	0.957	0.0945

Table 3.2: Coefficients for $G_2(S)$.

A_2	z_1	z_2	$1/\omega$	$2\xi/\omega$	p_1
801	0.157	-1.586	0.064	0.422	0.102

2. *Relaxation.* In this phase the system can be described as a *non-minimum phase system* ([14]). The associated transfer function is written on the same form of Eq 3.1 but, as shown in table 3.2, the presence of a zero with a positive real part, leads to an unstable function when the functin is inverted. For this reason the unstable part has been approximated with a 128th order

FIR filter, necessarily leading to a delayed response in time, as in [15]:

$$\frac{1}{N(z)} \approx F(z) \tag{3.2}$$

The higher the filter order, the better the approximation. Coefficients of $F(z)$ are extracted using the convergence properties of the geometrical series:

$$\lim_{N\to\infty} \sum_{k=0}^{N} (a)^k = \frac{1}{1-a} \qquad \forall\, a \text{ so that } |a| < 1 \tag{3.3}$$

Letting:

$$\frac{1}{N(z)} = \frac{1}{1 - z_i z^{-1}} \tag{3.4}$$

$$F(z) = \sum_{k=0}^{N} \gamma_k (z^{-1})^k \tag{3.5}$$

convergence is assured with $|z| > |z_i|$ if we choose the coefficients γ_k such that:

$$\gamma_k = z_i^k \tag{3.6}$$

Each function has been written in discrete-time notation using the polynomial form and the *Matlab* backward shift operator q[3]. For the extending phase the following equation has been used:

$$A_1(z)y(t) = B_1(z)u(t)$$

with

$$A_1(z) = 1 - 1.992\, z^{-1} + 0.9925\, z^{-2}$$
$$B_1(z) = 1 - 2.962\, z^{-1} + 2.925\, z^{-2} - 0.9627 z^{-3}$$

---

[3] Where $q^k\, u(t) = u(t-k)$.

whereas for the relaxation phase the following FIR filter has been calculated:

$$F(z) = \sum_{k=0}^{128} \gamma_k (z^{-1})^k$$

whose coefficients are:

$$\gamma_k = -0.1484 * 1.016^k$$

in series with the polynomial form:

$$A_2(z)y(t) = B_2(z)u(t)$$

with

$$\begin{aligned} A_2(z) &= 1 - 0.9984\, z^{-1} \\ B_2(z) &= 1 - 2.934\, z^{-1} + 2.869\, z^{-2} - 0.9352 z^{-3} \end{aligned}$$

3.2.3 MEMS accelerometers

Inertial sensors, especially accelerometers, are suitable for monitoring daily life activities due to their small dimensions, weight, low power supply and the useful information they provide about movement. Actually, these devices are currently used in clinical applications as actigraphs, for the measurement of the so-called circadian rhythm ([16]).

In this study we used LIS3L02AL Micro Electro - Mechanichals Systems (MEMS), representing a good fit for the development of unobtrusive devices: the same silicon substrate contains both sensor and electronic interface. Figure 3.6 shows the device employed. A special padded belt has been used to support the accelerometer in order to minimise the motion artifact in flexion due to skin displacements above spinous processes.

An inertial accelerometer implementing a mass, spring and damper model, which is subjected to an external force F_{ext} in an inertial reference frame, is driven by the Newton's law:

$$kx + b\dot{x} + m\ddot{x} = m\ddot{x}_{ext} \tag{3.7}$$

that is, using Laplace transform:

$$kX(s) + sbX(s) + ms^2X(s) = ms^2X_{ext}(s)$$

from which the following relation:

$$\frac{X(s)}{s^2X_{ext}(s)} = \frac{m}{ms^2 + sb + k} \tag{3.8}$$

Eq. 3.8 is the transfer function between acceleration and displacement. Let $\omega_n \triangleq \sqrt{\frac{k}{m}}$ be the cut frequency and $\xi \triangleq \frac{b}{2\sqrt{km}}$ the damping factor, then we obtain the following relation:

$$\frac{X(i\omega)}{A(i\omega)} = \frac{1/{\omega_n}^2}{(i\omega/\omega_n)^2 + 2(i\omega)\xi/\omega + 1} \tag{3.9}$$

from which we derive that when $\omega \ll \omega_n$ acceleration is proportional to displacement by the following relations:

$$A(i\omega) = {\omega_n}^2\, X(i\omega) \tag{3.10}$$

$$a(t) = {\omega_n}^2\, x(t) \tag{3.11}$$

where $1/{\omega_n}^2$ represents the device sensitivity.

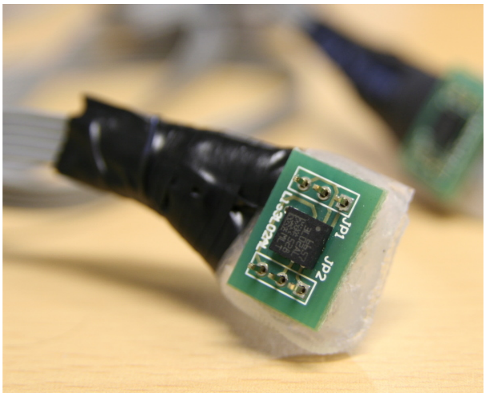

Figure 3.6: Integrated triaxial accelerometer LIS3L02AL and its connection to the system.

If the acceleration is small compared to the gravity, the accelerometer can be used as an inclinometer. This assumption may be valid under quasistatic conditions like the measurement of sway, but is violated during dynamic tasks such as lifting or quick-paced walking. In this analysis, we worked under the hypothesis of small accelerations and the validity of this assumption is discussed in Sec. 3.4.

3.2.4 Accelerometer placement

As in Fig. 3.7, a couple of accelerometers has been placed in proximity of the sacrum and on the spinous prominence of the T12 thoracic vertebra. The same figure shows the notation used. As said in Sec. 3.2.3, the inertial devices has been used exclusively as inclinometers: flexion-extension is determined reading the $\Delta\varphi$ angle, that is the angular difference between the gravity vector and both z axis of

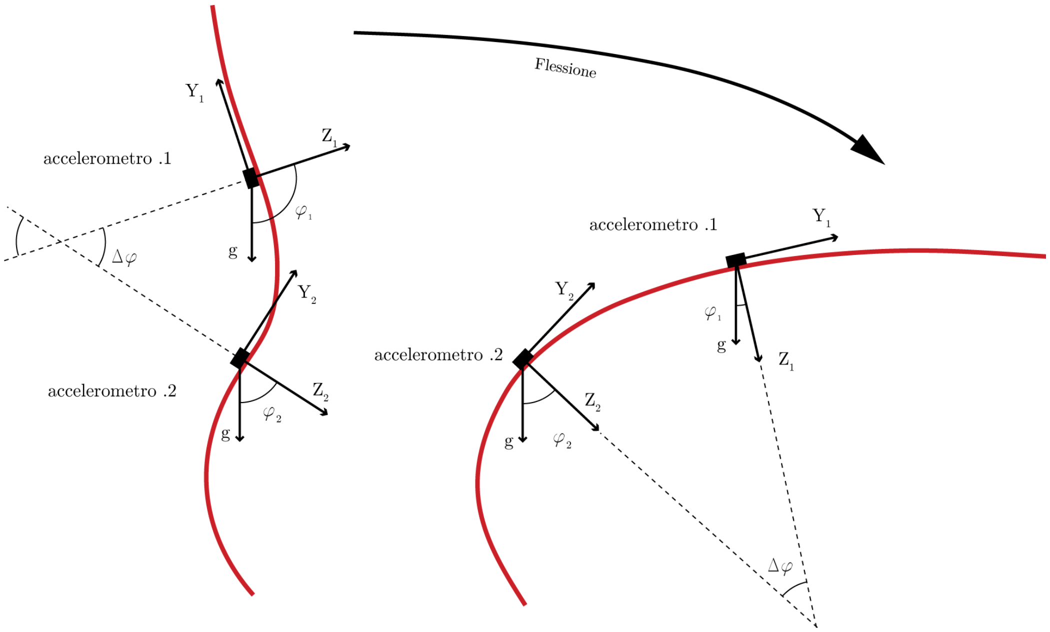

Figure 3.7: Accelerometer placement and measuring notation in the sagittal plane.

sensors.

For each accelerometer the following values where processed:

$$P_n = \sqrt{x_n^2 + y_n^2} \tag{3.12}$$

$$R_n = \sqrt{P_n^2 + z_n^2} \tag{3.13}$$

$$\theta_n = atan2(y_n, x_n) \tag{3.14}$$

$$\varphi_n = atan2(P_n, z_n) \tag{3.15}$$

where R represents the acceleration module. The $atan2(x, y)$ function is defined as: with $y \neq 0$

$$\text{atan2}(y, x) = \begin{cases} \varphi \cdot \text{sgn}(y) & x > 0 \\ \frac{\pi}{2} \cdot \text{sgn}(y) & x = 0 \\ (\pi - \varphi) \cdot \text{sgn}(y) & x < 0 \end{cases} \tag{3.16}$$

where φ is the angle such $\tan(\varphi) = \left|\frac{y}{x}\right|$ and sgn is the sign function, otherwise

$$\text{atan2}(0, x) = \begin{cases} 0 & x > 0 \\ 0 & x = 0 \\ \pi & x < 0 \end{cases} \tag{3.17}$$

In this way the *atan*2 function gives the counterclockwise angle between a vector and the x axis overcoming the singularities of the simple *atan* function. The angle φ is so calculated as:

$$\Delta\varphi = \varphi_1 - \varphi_2 \tag{3.18}$$

Figure 3.8 shows the Simulink model used to process accelerometer data, where *cartesian to spherical* blocks has been used to implement equations 3.13,3.14 and 3.15.

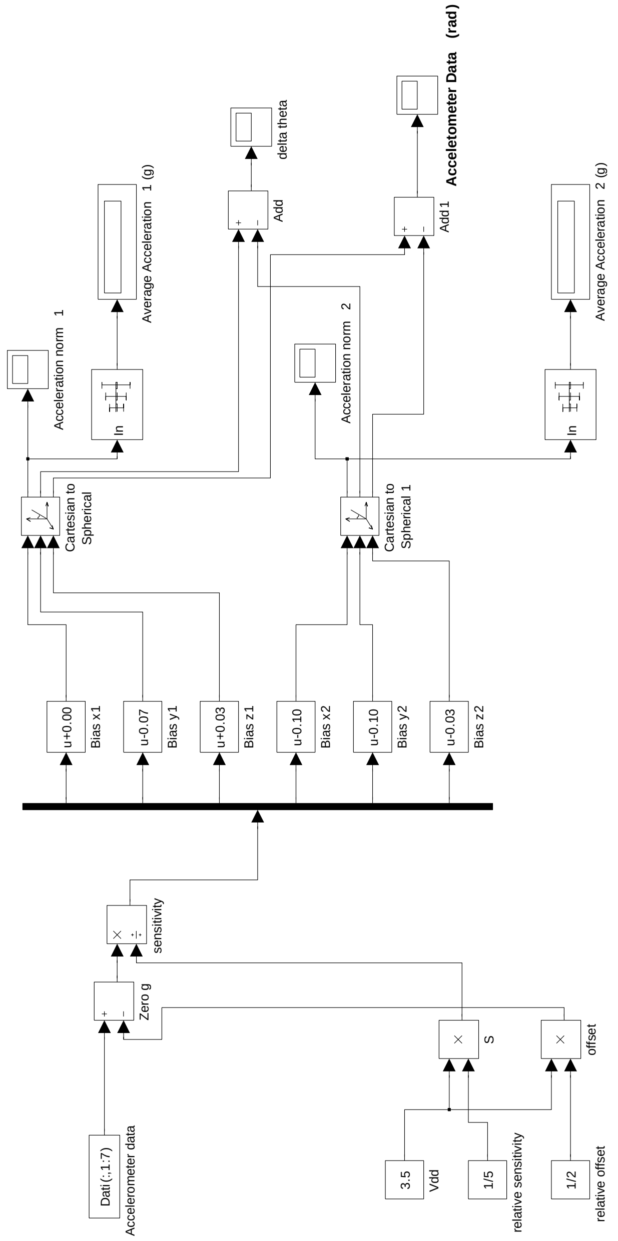

Figure 3.8: Simulink accelerometer model.

3.3 Sensory fusion experiment

The whole system has been tested in the FIGC Motion Lab of Coverciano (Firenze, Italy) using the *BTS Elite*[4] stereophotogrammetic motion capture system as external reference system for experimental validation. Figures 3.9, 3.10(a) and 3.10(b) describe the setup.

A single subject wearing the sensorized garment was asked to perform the following eight trials of different flexion-extension tasks that has been recorded and processed:

1. Preliminary test for link setup and synchronisation.
2. Series of two complete ROM flexion-extensions in one minute.
3. Random movements.
4. Very slow cycle of flexion-extension.
5. Rough flexion followed by a rough extension.
6. Same as 4.
7. Random movevents of trunk in the sagittal plane.
8. Same as 7.

During those tasks the distance between each marker has been recorded and the total length L_{tot} between marker 1 and 5 has been assumed as reference for lumbar arch (see Fig. 3.11). The purpose

---

[4] The *BTS Elite* is a 3D motion capture system composed of up to 16 infrared cameras, each one with 0,44 Mpixel of resolution and a frame rate of 120 fps. The declared sensitivity is 1/2800 of the observed field.

Figure 3.9: Sensorized prototype with CEs, accelerometers and *Elite* (BTS, Italy) optical markers.

was to compare the output of the hybrid multisensory model in respect to CEs raw data during the same trials and for this reason markers skin artifacts have not been accounted in this analysis.

The multisensory model is reported in Fig. 3.12: Data acquired from the whole system is processed splitting the CE signal in the two blocks as described in Sec. 3.2.2, while the accelerometer parameter is calculated and used as switch. In the meanwhile the *BTS Elite* length parameter is calculated.

Results are discussed in Sec. 3.4.

3.4 Results and discussion

Figure 3.13 shows the output of trials nr. 2 and nr. 4. It can be noticed that the signal processed with the hybrid model is more

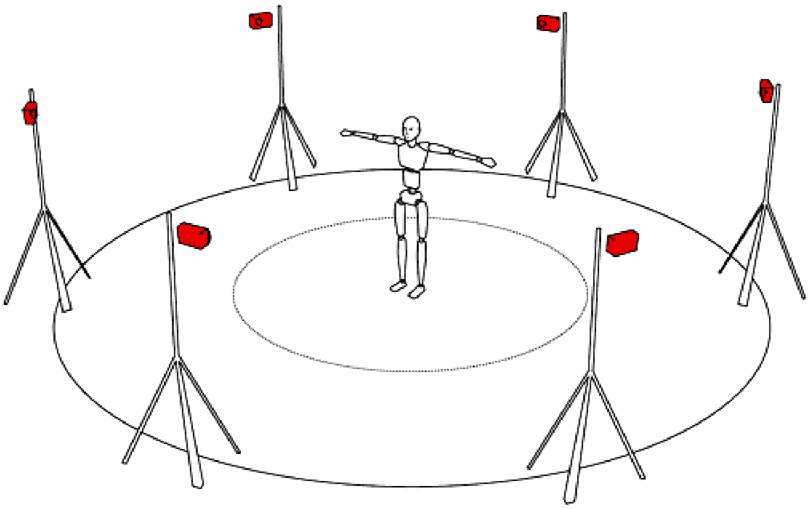

(a)

(b)

Figure 3.10: (a) The *BTS Elite* setup schema - (b) Calibration phase in the FIGC Motion Lab of Coverciano, Firenze (Italy).

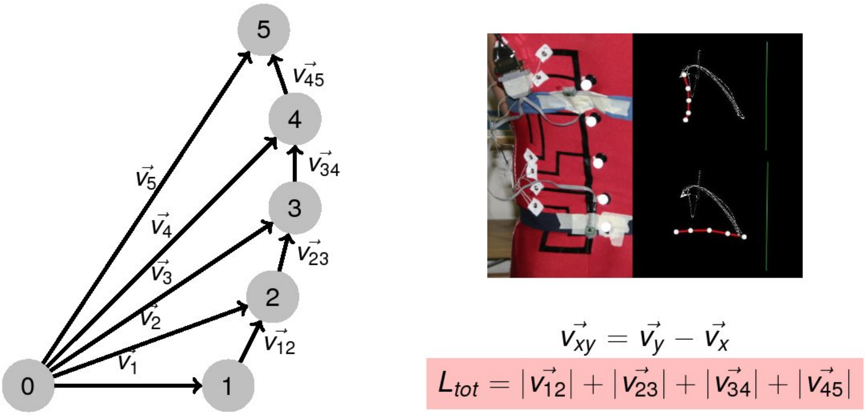

$$\vec{v_{xy}} = \vec{v_y} - \vec{v_x}$$

$$L_{tot} = |\vec{v_{12}}| + |\vec{v_{23}}| + |\vec{v_{34}}| + |\vec{v_{45}}|$$

Figure 3.11: Calculation of lumbar arch length L_{tot}.

adherent to the *BTS Elite* signal and the characteristic relaxation time of CE sensors is dramatically reduced with this analysis.

In order to avoid false switching of the hybrid model due to rough accelerations noises in the inertial sensors a cross-check block has been implemented, limiting the acceptable acceleration variation in a neighbourhood of the CE signal variation. This simple block resulted very reliable, augmenting the validity of a multisensory approach to such analysis.

In conclusion, the method proposed by [14] resulted a good approach for using CE sensors in wearable motion analysis, especially if the attention is focused to posture and gesture. The improvement of adopting a multisensory system overcome the single limitations of the technologies and resulted a robust concept, providing furthermore a way to crosscheck error scenarios.

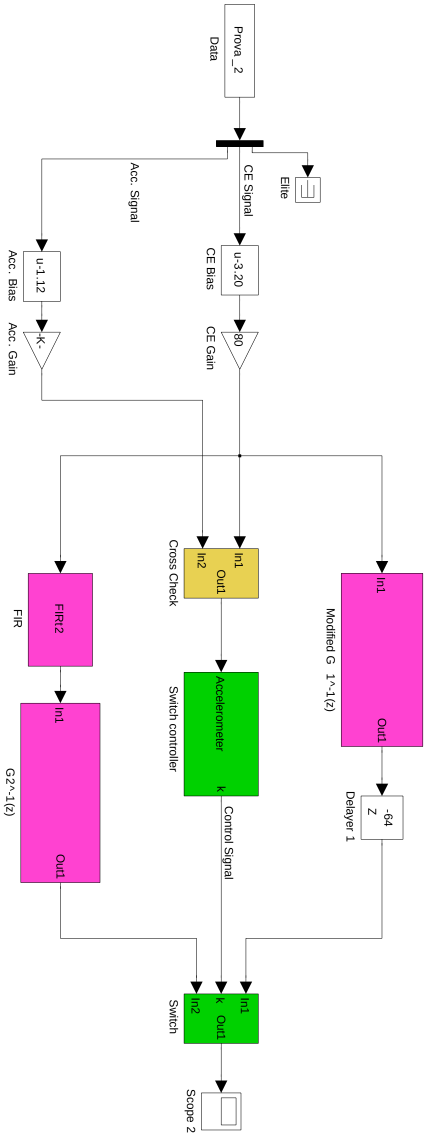

Figure 3.12: The *Simulink* multisensory model

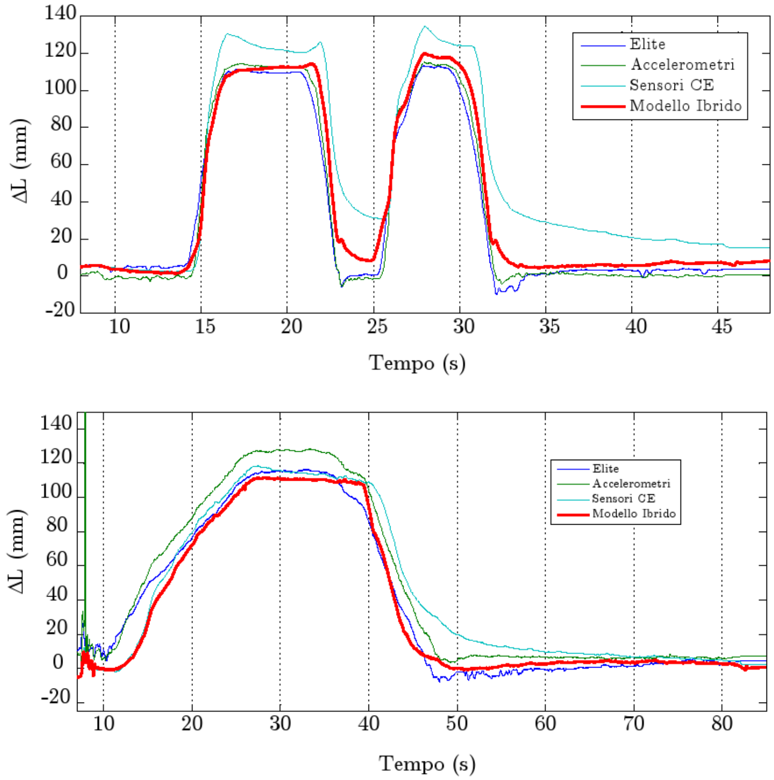

Figure 3.13: Outputs of trials nr. 2 and nr. 4 showing the calculated length of the lumbar arch with *BTS Elite*, raw CEs and with the hybrid model. In the same charts the normalised accelerometer signal is superimposed.

Table 3.3: Correlation coefficients of raw and processed signals in respect to the *BTS Elite* L_{tot} signal.

Trial N^o	CE raw	Hybrid model
2	0.9383	0.9850
4	0.9221	0.9661
5	0.8863	0.9014
6	0.9620	0.9868
7	0.8658	0.9401
8	0.8451	0.9312

Chapter 4

Smeared Conductive Elastomer Electrogoniometer

4.1 Introduction

This chapter introduces a method for detecting joint angles by using carbon loaded rubbers as piezoresistive strain sensitive materials. Materials used can be screen-printed onto fabrics to provide garments with a sensing apparatus able to reconstruct human postures and gestures. The main differences between this approach and the previous ones, and core of this work, is the rigorous proof that for small local curvatures of the layers constituting electrogoniometers, the resistance depends only on the total curvature of the layers and not on the particular form that the sensor keeps in adherence with human body. In this chapter we show that the hypothesis of small local curvature does not severely restrict the set of angles which can be detected.

Smeared redundant elastomer transducers SRETs have been employed, as strain sensors networks, to detect human posture and gesture. Elastic interconnection wiring is also easily realized leading to monolithic fabrication techniques which avoid the presence of metal wires and multiple solderings. Real time 3D reconstruction of body kinematics has been hard to obtain, since the advantages presented by SRETs inevitably lead to a strong dependence of the system performance by the body structure garment fitting. In few words, the skin (and covering fabric) stretching corresponding to different state of a joint differs from a subject to another, so the use of strain sensors adherent to skin has to be personalized according to the subject anthropometry. This problem has been solved by considering the human kinematic chain as a part of the system. By using identification algorithms, functions which relate joint angles to electrical values presented by the sensor network have been created. The construction of these functions is quite complex and time of computation dramatically increases with the number of degrees of freedom and with the accuracy required to the system to be resolved [12].

In the following the global curvature of a SRET layer will be related to the electrical resistance value variation and we will explore under which condition the resistance can be considered uncorrelated with its particular bending profile. The configuration proposed in this work is primarily aimed at reducing computational complexity and time of SRET networks as surface stretch sensor arrays. This result will ensure the possibility to detect different joint angles in different subject without accounting for the differences in body structure and with no subject calibration of the system. We call this device *Smeared Conductive Elastomer Electrogoniometer* (SCEEG). We intend here to analyze and test the feasibility of sensing structures which behave similarly to classical electrogoniometers being, however, fully compatible with industrial textile technology. The integration of SRET arrays and SCEEGs will definitely provide a powerful tool for human body posture and gesture reconstruction through efficient and fast algorithms. We show (in sections 4.2, 4.4), by both analytical results and simulations, that the geometrical properties of this device consent to measure angles with good accuracy even if the device undergoes deformations having bounded curvature, in particular we analyze the difference between a single layer and double layer system. Prototypes have been constructed and experimental trials performed (section 4.5). Obtained data have been analyzed statistically, confirming the theoretical results and the expected properties of the proposed electrogoniometric system.

4.2 Materials and device fabrication

In this study, specimens have been realized by directly casting WACKER's CE (3.2) in rectangular teflon moulds, obtaining samples having 200 mm length, 20 mm width and 1mm thickness. Moulds have been placed in an oven at a temperature of 130°C. During this phase the liquid compound cross-links and in about 10 minutes the sensing elements are ready to be employed (Fig. 4.2). Specimens have been tested by experimental trials to determine their electro-mechanical properties. Young modulus has been measured to be 0.1 GPa under quasistatic loading conditions. The specimens were stretched up to the length described in the first column of table 1, then electrical resistance was measured by the four point technique performed by a Keithley multimeter, by supplying the piezoresistive film with a 2 mA constant current. They show an initial electrical resistance of about 5 $k\Omega$ and a gauge factor of 1.96 ($GF = \frac{\Delta R L_0}{\Delta L R_0}$). The cross section of the sample at different extensions was calculated under the assumption of isovolumic deformation which is very reasonable for a rubbery material (Poisson ratio$\simeq$ 0.5). Resistivity values were calculated as:

$$\rho = R\frac{A}{l}$$

where R represents the electrical resistance, A the cross sectional area and l the length of the specimen. To neglect, with reasonable approximation, deformation of film extremities which locally change shape, electrical tests have been performed only on the central part of the sample (having a rest length of 100 mm) even if the total rest length of specimens were 200 mm.This provision also ensures that current lines in the tested segment are almost parallel.

The same trial has been repeated by injecting different current values (up to4 mA). Results of these experiments are summarized in Fig. 4.1. Non linearity in the ratio between applied voltage and injected current are relevant for large deformations (over 20%) and current greater than 3-3.5 mA, while the resistivity can be assumed constant under small deformations or low current, as in the cases we considered in this work.

The working principle behind the wearable, textile based sensors

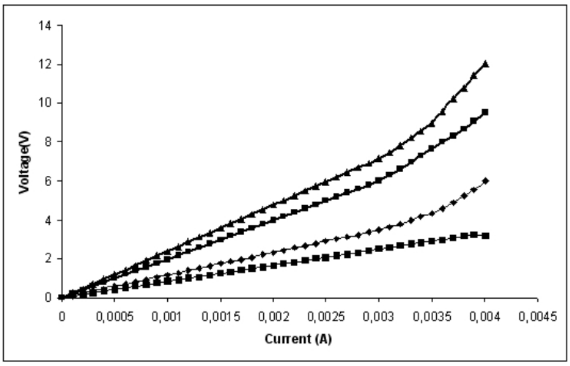

Figure 4.1: *Current injected in the CE and voltage drop for different extension of the film: a:* 20%, *b:* 15%, *c:* 10% *d:* 5%.

presented in this chapter is described in the following section. Sensors can be, in principle, realized into two alternative configurations, i.e. single and double layer benders. Our embodiment is conceived to be compatible with existing textile technology and easy to integrate into a garment. Since error estimation in the double layer configuration is predicted (see section 4.4) to be much lower, only sensors conform to it have been fabricated. To test the sensor performance and accuracy a preliminary embodiment was fabricated. Inextensible double layer devices have been fabricated by applying two identical conductive elastomeric film on a flexible substrate (polyvynil cloride resin VIPLA^{TM} biadhesive tape provided with acrylic adhesive) having a thickness of 0.1mm and a Young modulus of 15GPa. The Young modulus of the silicon rubber is about 0.1GPa so, even if the section of the rubber is larger than the substrate one, its bending stiffness can be neglected. A weldable copper tape (4mm width, 0.04mm thickness) has been used to realize electrical contacts on the

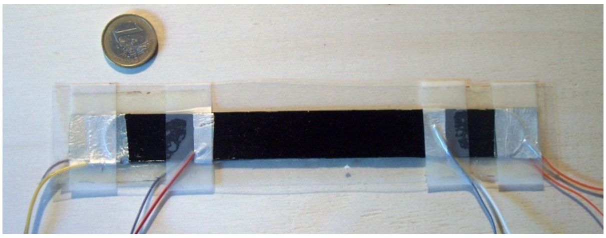

Figure 4.2: *The experimental setup.*

CE film, both for amperometric and for votmetric measurements (see Fig. 4.2).

In order to neglect boundary effects, the specimens we used to realize the system are longer than the portion we used to detect angle. During the assembly on the adhesive tape, a light pretensioning has been given to the two sensing layers in order to set equal rest resistances. This is the only calibration the device requires.

4.3 Methods

In this section we remark some geometrical properties of planar curves which are necessary to describe the electrical properties of a CE specimen under shape modification (Sec. 4.3.1). In Sec. 4.3.2 the electrical resistance of an inextensible elastomeric film under bending is explicitly computed as an analytic function of its local thickness. Moreover, electrical resistance is related to the global curvature assumed during bending. In Sec. 4.3.3, the electromechanical properties of a complete device, made of two CE coupled layers are analyzed and the mapping between global curvatures and changes in differential resistance is provided in an explicit (and efficient) form.

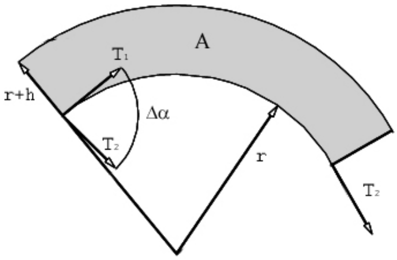

Figure 4.3: *A sector of circular crown and tangent vectors*

4.3.1 Geometrical properties of regular planar curves and notation

In this section some geometrical properties of differentiable curves and curvatures are remarked and we report some results to prove our assumption. A curve $x(t)$ in $\mathbb{R}^2$ is a function $\mathbb{R} \supset [t_0, t_1] \rightarrow \mathbb{R}^2$. $x(t)$ is *continuous, differentiable*, $C^1[t_1, t_2], C^2[t_1, t_2]$ if its components, seen as functions $\mathbb{R} \rightarrow \mathbb{R}$ are *continuous, differentiable*, $C^1[t_1, t_2], C^2[t_1, t_2]$, respectively. If $x(t)$ is differentiable at $t_0 \in [t_1, t_2]$, the vector tangent to $x(t)$ in t_0 corresponding to the parameter t is defined as the derivative $\mathbf{T(t_0)} = \mathbf{[dx_1(t)/dt, dx_2(t)/dt]^T}$. A curve $x(s)$ is said *parametrized in normal form* if s is its arc length, i.e. $\|\mathbf{T(s)}\| = 1$ for each $s \in [s_1, s_2]$. If $\mathbf{T(s)}$ is differentiable, it is possible to define the *curvature* $k(s)$ of a curve as

$$k(s) = \left\| \frac{d\mathbf{T(s)}}{ds} \right\|_2$$

where $\| \, . \, \|_2$ represents the canonical $\mathbb{R}^2$ norm. The subscript symbol $_2$ will be omitted in the following. It is easy to prove that if $k(s)$

is the curvature of a curve in normal form $x(s) : [s_1, s_2] \to \mathbb{R}^2$, the quantity:

$$\Delta\alpha = \int_{s_0}^{s} k(s)\ ds \tag{4.1}$$

represents the angle between the tangent vectors $\mathbf{T(s_0)}$ and $\mathbf{T(s)}$, $s_0, s \in [s_1, s_2]$. In fact, let us consider the quantity (see also Fig. 4.3)

$$\|\mathbf{T(s_0)} - \mathbf{T(s)}\| = 2\ \sin\left(\frac{\Delta\alpha}{2}\right) = \Delta\alpha + O(\Delta\alpha).$$

When $s \to s_0$, said $s - s_0 = \Delta s$, we have:

$$k(s) = \lim_{\Delta s \to 0}\left\|\frac{\mathbf{T(s_0)} - \mathbf{T(s)}}{\Delta s}\right\| = \lim_{\Delta s \to 0}\frac{\Delta\alpha + O(\Delta\alpha)}{\Delta s}$$

$$= \lim_{\Delta s \to 0}\frac{\Delta\alpha}{\Delta s}\left(1 + \frac{O(\Delta\alpha)}{\Delta s}\right) = \frac{d\alpha}{ds}$$

which prove equation (4.1), also for $s_0 = s_1$ and $s = s_2$.
In this sense, $\Delta\alpha$ can be considered as the *total curvature* of $x(s)$ between s_1 and s_2.

We want to show that for large curvature radii of the elastomeric film (i.e. at each point the local curvature $k(s)$ of the film is small enough if compared with the curve length and the thickness of the rubber sensor), we obtain a direct relation among the film total resistance and its total curvature. In order to do that, we will consider an elastomeric film as a cylinder whose base is the face parallel to the plane in which the bending occurs. In this way, the treatment is reduced to a planar problem and the curve $x(s)$ has to be regarded as one side of the intersection of the film with the plane where the bending occurs. In order to prove our statement, let us recall that the canonical C^2 norm of a curve defined on a interval $[s_1, s_2]$ is defined as:

$$\|x(s)\|_{C^2} = \sup_{s\in[s_1,s_2]} \|x(s)\| + \sup_{s\in[s_1,s_2]} \left\|\frac{dx(s)}{ds}\right\| + \sup_{s\in[s_1,s_2]} \left\|\frac{d^2x(s)}{ds^2}\right\|. \tag{4.2}$$

The next result, concluding this subsection, completes the properties of $C^2[s_1, s_2]$ curves necessary to our treatment and will be fundamental in relating total curvature and resistance of an elastomeric film. It substantially states that *each C^2 curve can be approximated in the C^2 norm by curves constituted by the union of finite sequences of circle arcs* and it allow us to substitute any curve with a corresponding one having simpler geometrical properties. Let us remark that a curve made of circle arcs is not C^2, unless all circles have the same curvature. These curves however have sudden discontinuities at points where different circles merge. To formalize the needed result and include these kind of curves let us then consider a small modification to the above C^2 norm. If a curve is C^1 and piecewise C^2, such that at each point the right and left second derivatives $\left(\frac{d^2x(s)}{ds^2}\right)^+$ and $\left(\frac{d^2x(s)}{ds^2}\right)^-$ exist, consider the expression:

$$\|x(s)\|_{C^{2+-}} = \sup_{s\in[s_1,s_2]} \|x(s)\| + \sup_{s\in[s_1,s_2]} \left\|\frac{dx(s)}{ds}\right\| \tag{4.3}$$

$$+ \sup_{s\in[s_1,s_2]} \left\|\left(\frac{d^2x(s)}{ds^2}\right)^+\right\| + \sup_{s\in[s_1,s_2]} \left\|\left(\frac{d^2x(s)}{ds^2}\right)^-\right\|.$$

The proof that $\|x(s)\|_{C^{2+-}}$ is a well defined norm is trivial since the defining relationship is subadictive. By using this new function it is possible to enunciate the following:

Lemma 1 *Let* $x(s)$ *be a* $C^2[s_1, s_2]$ *curve parametrized by arc length. Then, chosen* $\epsilon > 0$ *there is a finite set* $\{t_i\}_{i \leq n}$ *with* $t_1 = s_1, t_n = s_2$ *such that* $\bigcup_{i=1}^{n}[t_i, t_{i+1}] = [s_1, s_2]$ *and arc length parametrized circle arcs* $\{\gamma_1, ..\gamma_n\}$*,* $\gamma_i : [t_i, t_{i+1}] \to \mathbb{R}^2$*, such that the curve resulting by the union of the arcs*

$$\gamma(t) = \gamma_i(t) \text{ if } t \in [t_i, t_{i+1}] \tag{4.4}$$

is C^1 *and*

$$\|x(s) - \gamma(s)\|_{C^{2+-}} < \epsilon. \tag{4.5}$$

The proof of the previous statement can be found in section 4.7.

4.3.2 Total electrical resistance of an elastomeric film as a function of the local thickness

In the following we will assume some properties of the elastomeric film which account both for the volume symmetries of the material and the continuity of their properties under limited bending. In particular:

i. the elastomer is mechanically isotropic and its deformation isovolumic;

ii. the side of the specimen which matches with the curve $x(s)$ is inextensible;

iii. if the curve $x(s)$ is a circle arc then the elastomeric film forms a circular crown;

iv. the elastomeric film shape and its electrical resistance R_x depend only on the curve $x(s)$ and this dependence is continuous in the C^{2+-} norm, i.e. chosen $\delta > 0$ there exists $\epsilon > 0$ such that if $\|x_1(s) - x_2(s)\| < \epsilon$ then $|R_{x_1} - R_{x_2}| < \delta$;

v. if the union of two curves $x_1(s), x_2(s)$ forms a C^1 curve $x_1 \cup x_2$, then $R_{x_1 \cup x_2} = R_{x_1} + R_{x_2}$;

vi. the elastomeric film is electrically homogeneous and isotropic.

Let us consider the film in flat position, i.e. when the curve $x(s)$ is a (straight) segment. In this configuration, we indicate by h_0 the thickness of the elastomeric film, which unchanges along all the length of $x(s)$, and we consider a small segment $x'(s) = [x(s_{1'}), x(s_{2'})] \subset [x(s_1), x(s_2)]$ having length $l = s_{1'} - s_{2'}$.

In the following we will suppose that the width of the elastomeric film is unitary, and that the behavior of the material on parallel planes orthogonal both to $x(s)$ and to the curvature direction is the same. Under this hypothesis, the volume of the elastomeric material in the cylinder between $x(s_{1'})$ and $x(s_{2'})$ is $V = h_0 l$.

Let us now bend the device in order to transform $x'(s)$ into a circle arc having total curvature $\Delta\alpha$ and radius $r = l/\Delta\alpha$. By hypothesis (iii) the film is mapped into a circular crown having R as the radius of the side opposite to x'. Note that R can be greater or smaller than r, since no assumptions have been made on the sign of the curvature. The area A of the considered disc sector is given by (see Fig. 4.3) $A = \frac{\Delta\alpha}{2}(R^2 - r^2)$ or $A = \frac{\Delta\alpha}{2}(r^2 - R^2)$ and by assumption (i), $h_0 l = A$.

Let us also indicate as $h = |R - r|$ the actual thickness of the film after bending. Moreover, let us remark that this notation implies $\Delta\alpha = l/r$.

Hence $h_0 l = \frac{l}{2r}(R^2 - r^2)$ or $h_0 l = \frac{l}{2r}(r^2 - R^2)$ according to the direction of bending, which provide the relationships

$$h_0 = \frac{1}{2r}((r+h)^2 - r^2) \tag{4.6}$$

or

$$h_0 = \frac{1}{2r}(r^2 - (r-h)^2), \tag{4.7}$$

respectively. Both equation (4.6) and equation (4.7) have two solutions. For each one, a solution has an essential discontinuity for $\frac{1}{r} \to 0$ (or alternately $r \to \infty$) and cannot be used for small bending. The other two solutions, evaluated for $k = 1/r$, are undefined in $k = 0$, but they can be continuously extended. So by solving with respect to h we have:

$$h = -\frac{1}{k} + \sqrt{\frac{1}{k^2} + \frac{2h_0}{k}} \tag{4.8}$$

and

$$h = -\frac{1}{k} + \sqrt{\frac{1}{k^2} - \frac{2h_0}{k}} \tag{4.9}$$

for relation (4.6) and (4.7), respectively.

Solutions (4.8) and (4.9) can be continuously extended in $k = 0$ and they can be, respectively, expanded in Taylor's series as follows:

$$h = h_0 - \frac{1}{2}h_0^2 k + \frac{1}{2}h_0^3 k^2 - \frac{5}{8}h_0^4 k^3 + O(k^4) \tag{4.10}$$

and

$$h = -h_0 - \frac{1}{2}h_0^2 k - \frac{1}{2}h_0^3 k^2 - \frac{5}{8}h_0^4 k^3 + O(k^4). \tag{4.11}$$

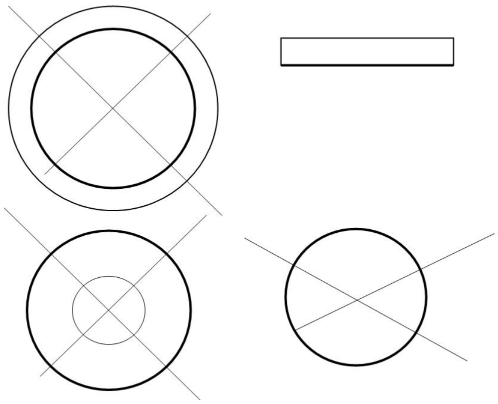

Figure 4.4: *Cases of circular bending of a specimen when the length of one side does not change*

It is important to stress out that the signs of odd terms are opposite. This result will be used in section 4.3.3. Moreover, the two solutions correspond to the same degree of bending of the film in opposite directions under the hypothesis that the length l of $x'(s)$ remains unchanged. Equation (4.6) is defined for $k > -\frac{1}{2h_0}$. In particular, for $k > 0$ the considered film is "convex" (with respect to the inextensible arc, Fig. 4.4, case a) and $|h| < |h_0|$, for $k = 0$ the specimen is straight and $h = h_0$ (case b), for $-\frac{1}{2h_0} < k < 0$ the film is "concave" (c) and $|h| > |h_0|$, and for $k = -\frac{1}{2h_0}$ the film bending "saturates" and the circular crown degenerates into a circle sector (d). This limit corresponds to $\alpha = l/h_0$ total bending. Similar considerations can be made also for equation (4.7). We will not investigate, in the present work, the cases where the circular crown degenerates.

In the remaining part of this section we show how the electrical resistance of a bent film can be computed. According to hypothesis (vi), the material is electrically homogeneous and the film can be considered as a sector having angular measure $\Delta\alpha = kl = k(s_{2'} - s_{1'})$ of a Corbino's disk [17], whose radial resistance can be computed as:

$$R_c = \frac{\rho k l}{\log(\frac{r_M}{r_m})} \tag{4.12}$$

where r_M and r_m are the major and the minor radii of the circular crown. Since (4.8) and (4.9) provide an explicit dependence of r_M and r_m on k and h_0, equation (4.12) states that the resistance R_c of the elastomeric film standing on a small arc of circle measured between its extremities only depends on the resistivity of the material ρ, on the length l of the arc, on the thickness of the film h_0 evaluated in flat position and on the curvature k. In particular, equation (4.12), specialized using (4.8) and (4.9) becomes

$$R_c^+ = \frac{\rho k l}{\log(\sqrt{1 + 2h_0 k})} \tag{4.13}$$

and

$$R_c^- = -\frac{\rho k l}{\log(\sqrt{1 - 2h_0 k})} \tag{4.14}$$

Relations (4.13) and (4.14), as well as (4.8) and (4.9) present removable discontinuities in $k = 0$. Moreover, both the limits of the two functions and the ones of all their derivatives exist. They can be expanded by using Taylor's formula and we obtain:

$$R_c^+ = \frac{\rho l}{h_0} + \rho l k - \frac{1}{3}\rho l h_0 k^2 \tag{4.15}$$

$$+\frac{1}{3}\rho l h_0^2 k^3 - \frac{19}{45}\rho l h_0^3 k^4 + O(k^5)$$

and

$$R_c^- = \frac{\rho l}{h_0} - \rho l k - \frac{1}{3}\rho l h_0 k^2 \qquad (4.16)$$

$$-\frac{1}{3}\rho l h_0^2 k^3 - \frac{19}{45}\rho l h_0^3 k^4 + O(k^5)$$

Relations (4.15) and (4.16) stress out that the resistance of a circle arc is given by the resistance of the specimen in flat position increased or decreased by a quantity (according to the bending versus) depending on k. It is important to point out that in the Taylor‘s expansions of R_c^+ and R_c^-, the absolute values of all corresponding terms are equal. Zero-order and even-order terms have the same signs while odd-order terms have opposite signs. This result will be employed in section 4.3.3 in order to conceive a improved system to detect angles. Finally, if we consider the Taylor’s expansion truncated to the first order term, by recalling that $lk = -\Delta\alpha$ (according to a choosen convention between the two possibles on curvature sign) we obtain for (4.15)(and likewise, for (4.16))

$$R_c^+ = \frac{\rho l}{h_0} - \rho\Delta\alpha + O(k^2) \qquad (4.17)$$

which states the explicit dependence between the total curvature and the electrical resistance and can be applied for small curvature bending. Let us conclude this section by computing the relationship between the resistance of a bent film and its global curvature. Consider a film bent according to a deformation of its inextensible profile $x(s)$. Fixed $\delta > 0$, by using lemma 1, it is possible to chose a set of circle arcs $\{\gamma_1(s_1), ..\gamma_n(s_n)\}$, having curvatures $k_1, ..k_n$, which satisfy the assumption (iv). The resistance of the film having $\gamma(s) = \cup_{i=1}^{n}\gamma_i(s_i)$ as its inextensible profile is given (according to the curvature sign, or concavities) by

$$R_c = \sum_{i=1}^{n_1} \frac{\rho k_i l_i}{\log(\sqrt{1+2h_0 k_i})} + \sum_{i=n_1}^{n} -\frac{\rho k_i l_i}{\log(\sqrt{1-2h_0 k_i})}$$

$$= \sum_{i=1}^{n} \left(\frac{\rho l_i}{h_0} - \rho \Delta\alpha_i \right) + O(\sup_{i\leq n} k_i^2) \tag{4.18}$$

with

$$|R_{x(s)} - R_c| < \delta \tag{4.19}$$

where the curvature is chosen to be positive in the segments from indexed from 1 to n_1 and $\Delta\alpha_i$ are considered with their signs, according to the concavity or convexity of the curve $x(s)$. We remark that in equation (4.18), the possibility to choose a C^1 curve and C^{2+-} approximations is a crucial point because, in order to sum each single contribution to the total curvature, the tangent vector in an extremity of an arc has to coincide with the tangent vector in the correspondent point of the next arc (see assumptions iv and v).

Now, by lemma 1 the curve $x(s)$ can be better and better approximated by a sequence of curves made of circular arcs. As the approximation becomes more and more accurate when the number of arcs increases, possibly going to infinity, while the arc lengths become zero. By assumption (iv), equation (4.18) becomes:

$$R_{x(s)} = \int_{S_1} \frac{\rho k(s) ds}{\log(\sqrt{1+2h_0 k(s)})} + \int_{S_2} \frac{\rho k(s) ds}{\log(\sqrt{1-2h_0 k(s)})}$$

Here S_1 is the subset of $[s_1, s_2]$ where $x(s)$ is "‘convex"’ and S_2 is the subset of $[s_1, s_2]$ where $x(s)$ is ‘concave’. Then

$$R_{x(s)} = \int_{S_1} \frac{\rho}{h_0} + \rho k(s) + ...\, ds + \int_{S_2} \frac{\rho}{h_0} - \rho k(s) + ...\, ds = \tag{4.20}$$

$$= (s_2 - s_1)\frac{\rho}{h_0} - \rho\,\Delta\alpha + O(\sup_{s \in S_1 \cup S_2} k(s)^2)$$

which proves that first order term of the total resistance is the total curvature as we wanted to prove.

4.3.3 Double layer goniometric system

In previous section we proved that the variation of the electrical resistance of an inextensible elastomeric piezoresistive film undergoing bending is related to the local curvature of the inextensible side and, with a certain approximation, to the difference between the tangent vectors to the film in its extremities. The approximation we obtain is a first order Taylor's expansion which holds for small values of the local curvature. In this section we want to improve this result by presenting a film configuration which cancels the second order term of the Taylor's series, ensuring that the errors involved in evaluating angles through electrical resistance are, at least, a third order function of $sup(k(s))$.

Let us consider a double layer system (such as the one represented in figure 4.5) where two identical elastomeric films are fixed on the two opposite sides of a flexible and inextensible substrate. Let us suppose that the thickness of the substrate is negligible with respect to the thickness of the layers and consider the difference of resistances

$$\Delta R_x = \Delta R_x^1 - \Delta R_x^2$$

obtained by subtracting the resistance value of the layer 1 from the resistance value of the layer 2. In case of an arch circle for the substrate, which according to our hypothesis corresponds to $x(s)$,

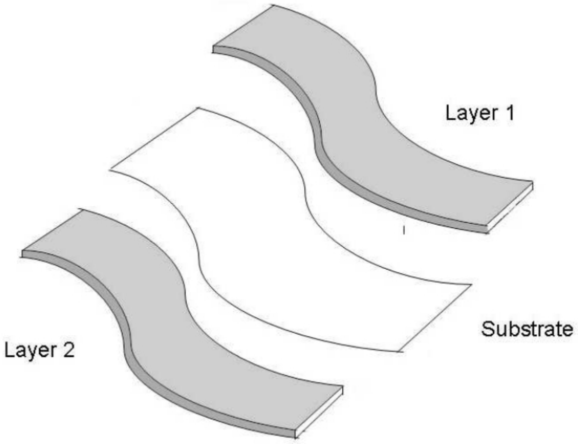

Figure 4.5: *A double-layer sensing system*

the parameter which characterizes the two elastomeric layers is the actual thickness h which is given by the two values expressed by expression (4.8) and (4.9). According to equations (4.13) and (4.14), we obtain:

$$\begin{aligned}\Delta R_c &= \frac{\rho k l}{\log(\sqrt{1+2h_0 k})} + \frac{\rho k l}{\log(\sqrt{1-2h_0 k})} \\ &= 2\rho l k + \frac{2}{3}\rho l h_0^2 k^3 + O(k^5) \qquad (4.21) \\ &= 2\rho\Delta\alpha + \frac{2}{3}\rho l h_0^2 k^3 + O(k^5).\end{aligned}$$

Equation (4.21) holds only for $-\frac{1}{2h_0} < k < \frac{1}{2h_0}$, but it does not contain any k-second order terms. On the other side, it is important to stress out that, while a single layer system works for an unbounded (in one direction, at least) range of k, curvature in double layer systems is comprised in a limited set. With the same notation of last section, this relation can be generalized to a any shape curve $x(s)$.

$$\Delta R_{x(s)} = \int_{S_1} \frac{\rho k(s) ds}{\log(\sqrt{1+2h_0 k(s)})} + \int_{S_2} \frac{\rho k(s) ds}{\log(\sqrt{1-2h_0 k(s)})}$$

$$-\int_{S_1} \frac{\rho k(s) ds}{\log(\sqrt{1-2h_0 k(s)})} - \int_{S_2} \frac{\rho k(s) ds}{\log(\sqrt{1+2h_0 k(s)})}$$

$$= \int_{S_1} \frac{\rho}{h_0} + \rho k - \frac{1}{3}\rho h_0 k^2 + \frac{1}{3}\rho h_0^2 k^3 - \frac{19}{45}\rho h_0^3 k^4 + O(k^5) ds$$

$$+ \int_{S_2} \frac{\rho}{h_0} - \rho k - \frac{1}{3}\rho h_0 k^2 - \frac{1}{3}\rho h_0^2 k^3 - \frac{19}{45}\rho h_0^3 k^4 + O(k^5) ds$$

$$- \int_{S_1} \frac{\rho}{h_0} - \rho k - \frac{1}{3}\rho h_0 k^2 - \frac{1}{3}\rho h_0^2 k^3 - \frac{19}{45}\rho h_0^3 k^4 + O(k^5) ds$$

$$- \int_{S_2} \frac{\rho}{h_0} + \rho k - \frac{1}{3}\rho h_0 k^2 + \frac{1}{3}\rho h_0^2 k^3 - \frac{19}{45}\rho h_0^3 k^4 + O(k^5) ds$$

$$= \int_{S_1} 2\rho k + \frac{2}{3}\rho h_0^2 k^3 + O(k^5) ds - \int_{S_2} 2\rho k + \frac{2}{3}\rho h_0^2 k^3 + O(k^5) ds$$

$$= 2\rho\Delta\alpha + \int_{S_1} \frac{2}{3}\rho h_0^2 k^3 + O(k^5) ds - \int_{S_2} \frac{2}{3}\rho h_0^2 k^3 + O(k^5) ds$$

$$= 2\rho\Delta\alpha + O(\sup_{s\in S_1\cup S_2} |k(s)|^3) \tag{4.22}$$

Although equation (4.20) and (4.22) look very similar, their meaning is quite different in terms of involved errors . In the next section, an explicit evaluation of the error in the two cases will be provided.

4.4 Error estimation in single and double layer configuration

4.4.1 Error and percentage error in single layer configuration

Let us consider the difference between the resistance value of a layer covering a circle arc (equation (4.13)) and its first terms in Taylor's expansion:

$$R_c^+ - \frac{\rho l}{h_0} - \rho l k = R_c^+ - R_{c_0}^+ - \rho\Delta\alpha = \tag{4.23}$$

$$-\rho l \frac{-2kh_0 + \log(1+2kh_0) + \log(1+2kh_0)kh_0}{\log(1+2kh_0)h_0}$$

Let us indicate

$$f(\phi) = \frac{-2\phi + \log(1+2\phi) + \log(1+2\phi)\phi}{\log(1+2\phi)} \tag{4.24}$$

It is possible to prove that

$$\lim_{\phi\to-\frac{1}{2}} f(\phi) = -\frac{1}{2} \quad \lim_{\phi\to\infty} f(\phi) = -\infty$$

and

$$f(0) = 0 \quad f\left(\frac{1}{2}\right) = \frac{1}{2}\frac{2-3\log(2)}{\log(2)}.$$

Moreover, by considering the derivative of f with respect to ϕ, it is possible to prove[1] that it is a growing function for $-\frac{1}{2} < \phi < 0$ and a decreasing function for $\phi > 0$. So, in order to estimate the

---

[1] by operating the substitution $\beta = \log(1+2\phi)$ the assertion is equivalent to $e^\beta > 1$ for $\beta > 0$.

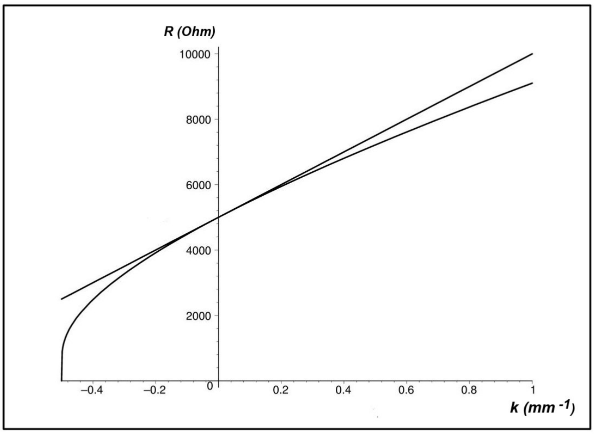

Figure 4.6: *Single layer device. Resistance value computed by Corbino's relation and resistance approximation (straight line) as a function of the angle* $\Delta\alpha$ *versus curvature k corresponding to* $\rho = 500\Omega \cdot mm$, $h_0 = 1\ mm$ *and* $l = 10\ mm$

error involved in evaluate angles by using equation (4.23) it will suffice to establish a zero's neighbour $[(-k_{Max}, k_{Max}) \subset [-\frac{1}{2}, +\infty)$ and evaluate the maximum error on its border. Moreover this result proves that, fixed a maximum curvature, k_{Max} the "worst" case, i.e. the largest error in angle evaluation for any film bending, is reached when the curvature is equal to k_{Max} at each point, that means that the curve $x(s)$ is a circle arc. In order to give an idea of the error in case of one-layer system, we present, as an example, the following numerical results. The right hand side of equation (4.23) is represented in figure 4.6 where we fixed $\rho = 500\Omega \cdot mm$, $h_0 = 1\ mm$ and $l = 10\ mm$ (and, implicitly, $1\ mm$ width).

Curvature $k = -0.5\ mm^{-1}$ (figure 4.4 (d)) produces an absolute

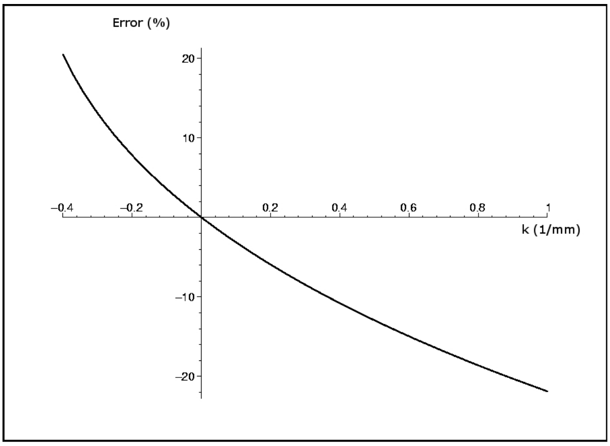

Figure 4.7: *Single layer device. Percentage error in angle evaluation for curvatures in* $[-0.4, 1]$ *with* $\rho = 500\Omega \cdot mm$, $h_0 = 1\ mm$ *and* $l = 10\ mm$

error of 2500 Ω (figure 4.6) which correspond to the 50% of the resistance initial value and makes the system unapplicable. For $k = -0.2\,mm^{-1}$ the error amounts to 85 Ω, while the resistance variation with respect to the flat position (where the error vanishes) is $R_c(0) - R_c(-0.2) = 1085\Omega$. $|k| = 0.2\,mm^{-1}$ and $l = 10\ mm$ correspond to a circle having radius equal to $5mm$. The total curvature (angle) is $|\Delta\alpha| = |k| \cdot l = 2\,rad \sim 115$ while, by computing $|\Delta\alpha^*|$ by Taylor's approximation we obtain

$$|\Delta\alpha^*| = \frac{1}{\rho}\left(R_c^+ - \frac{\rho l}{h_0}\right) = 2.17\,rad \sim 124^\circ. \tag{4.25}$$

In this case the error corresponds to 7.3% of the measured angle value (figure 4.7). Errors decrease while k increases and for $k = -0.1mm^{-1}$ we obtain an absolute error (in resistance) amounting to 19 Ω and a angle percentage error of about 3% For $k > 0$ the 10% percentage error is assumed at about $k = 0.4\,mm^{-1}$ which corresponds an angle $\Delta\alpha = 4\,rad \sim 230°$

4.4.2 Error and percentage error in double layer configuration

Things remarkably improve if we consider a double layer system. First, since $(R_c^+ - R_c^-)$ is defined only for $-\frac{1}{2h_0} < k < \frac{1}{2h_0}$ we have to compute:

$$\lim_{k \to -\frac{1}{2h_0}} R_c^+ - R_c^- = -\frac{\rho l}{h_0 \log(2)}$$

$$\lim_{k \to \frac{1}{2h_0}} R_c^+ - R_c^- = \frac{\rho l}{h_0 \log(2).}$$

Moreover in $k = 0$, $(R_c^+ - R_c^-)$ can be continuously extended by setting

$$(R_c^+ - R_c^-)_{k=0} = \lim_{k \to 0} R_c^+ - R_c^- = 0.$$

so it is continuous and bounded. It is possible to prove[2] that $R_c^+ - R_c^-$ is a increasing odd function on k. Fixed a maximum absolute value for the curvature $k_{Max} < \frac{1}{2h_0}$, the maximum error on the interval $[-k_{Max}, k_{Max}]$ is reached on its border. It can be quantified, in terms of resistance, by:

$$|\Delta R_c - 2\rho l k_{Max}| = \tag{4.26}$$
$$2\rho l k_{Max}\left(\frac{1}{\log(1 - 2k_{Max}h_0)} + \frac{1}{\log(1 + 2k_{Max}h_0)} - 1\right)$$

---

[2] as in the previous case, by differentiating and operating the substitution $\beta = \log(1 + 2h_0 k)$ the assertion is equivalent to $e^\beta > 1$ for $\beta > 0$.

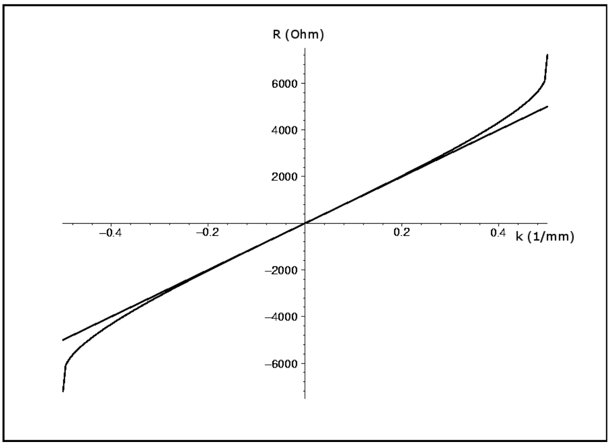

Figure 4.8: *Double layer device. Resistance value computed by Corbino's relation and resistance approximation (straight line) as a function of the angle* $\Delta\alpha$ *versus curvature* k *corresponding to* $\rho = 500\Omega \cdot mm$, $h_0 = 1$ mm *and* $l = 10$ mm *for a double layer system*

The absolute error in terms of voltage, given by relation (4.26) is represented in figure (4.8). It is clear how the infinitesimal second order error we commit greatly improve the system performance with respect to the one-layer one. For $k = -0.5\, mm^{-1}$ the error is larger than 4 radiants (the measured angle is 2 radiants) and the system is strongly inaccurate.

However, when $k = -0.2\, mm^{-1}$, which corresponds to 2 radiants ($\sim 114°$) the absolute error in terms of resistance amounts to -29Ω, which represents a percentage angle error of 4%. Finally, for $k = 0.1\ mm^{-1}$ ($\Delta\alpha = 1 rad \sim 57°$) the absolute error in resistance is smaller than 4Ω and the angle percentage error is smaller than 1%. Since in this case the error is an odd function, the same behavior holds for $k > 0$ (Fig. 4.9).

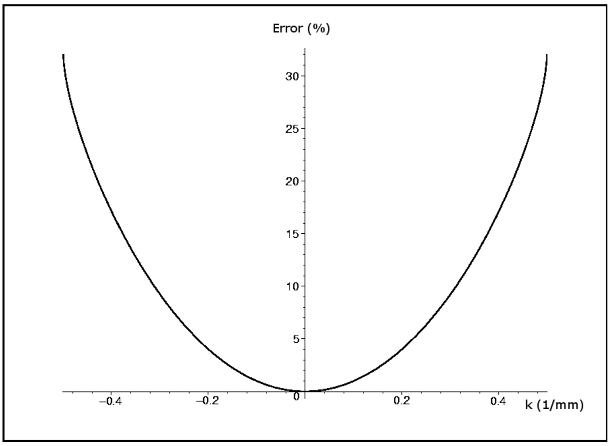

Figure 4.9: *Double layer device. Percentage error in angle evaluation for curvatures in* $[-0.4, 0.4]$ *with* $\rho = 500\Omega \cdot mm$, $h_0 = 1\ mm$ *and* $l = 10\ mm$ *for a double layer system*

4.5 Experimental results

The double layer sensor, whose fabrication procedure has been briefly described in section 4.2 has undergone two different types of test. The first one was aimed at proving that the difference of electrical resistance of the two layers during bending only depends, for small curvatures and, with reasonable accuracy, on the total curvature of the device. The trial has been iterated for different angles in order to provide a full characterization of the device behavior. We have fixed the extremities of the sensor, external to the voltmetric contact points, to a framework constituted by two rigid straight arms (Fig. 4.10).

A set of angles from 0 to 120° has been spanned by the two arms (positions have been imposed and measured by a SG150 elec-

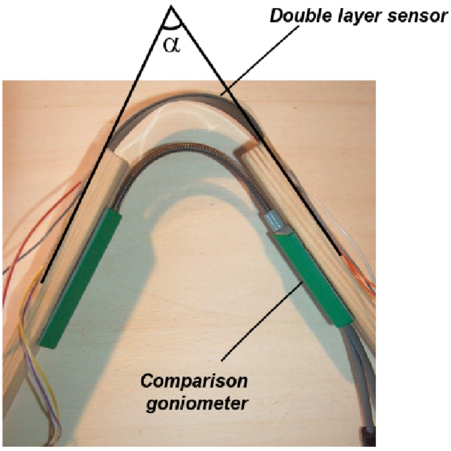

Figure 4.10: *A double layer device mounted on two rigid arms. The real angle is estimated by a laboratory electrogoniometer*

trogoniometer produced by Biometrics Ltd). In this way, the angles between the tangent vectors to the $(VIPLA^{TM})$ film corresponding to the voltmetric contact points assume the same values imposed to the framework. Layer resistances have been measured by a Keithley multimeter and angle estimation has been performed by using relation (4.22). In order to verify that the difference on resistance does not depend on the particular shape of the sensor in its central part, we have modified the shape of the supporting film by using a insulating small stick which kept the device in three different configuration (Fig. 4.11). Since the stick radius was $2.5mm$, the maximum curvature assumed by the system were $k_{Max} = 0.4\, mm^{-1}$. On the other hand, the minimal even curvature possible for the device in a position (characterized by the angle α) between the two arms of the framework is given by $k_{min} = \alpha/l$, and depends on the particular an-

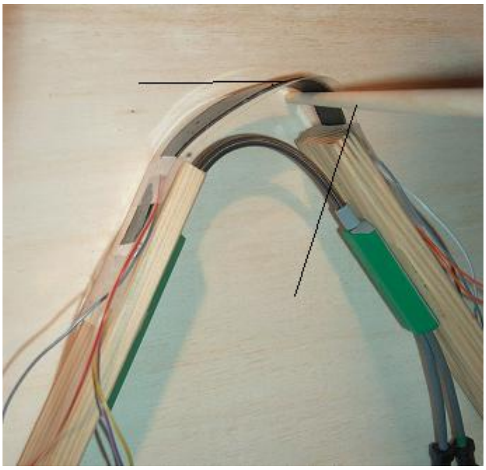

Figure 4.11: *The double layer device, perturbed by an insulated stick during the resistance acquisition*

gle measured. For these values of minimum curvature, the expected error when the films assume circle shapes is smaller than 1 %. The maximum curvature value is not negligible, but it is held only for a small length of the device. It is possible to suppose that the largest segment the device hold the maximum curvature is the half a length of the stick external circumference, i.e. $7.8\,mm$ which is expected to introduce an error of about 8° in the worst case (see section 4.4).

Results obtained are reported in table 2 where α represents the real angle imposed and measured via a commercial electrogoniometer, while (α_i, σ_i) are respectively the average values of the angle computed by the resistance differences on five acquisition for each considered position of the goniometer and the corresponding standard deviations. Groups (α_1, σ_1) and (α_2, σ_2) correspond to unperturbed and slightly perturbed status, while for (α_3, σ_3) the perturbation is larger.

Figure 4.12 shows the difference of resistance (and the standard deviation on five trials) between the two layers versus the angle assumed with a light disturbance performed by the stick, while figure 4.13 simultaneously shows the resistance differences versus the imposed angle under different perturbations.

α (°)	α_1 (°)	σ_1 (°)	α_2 (°)	σ_2 (°)	α_3 (°)	σ_3 (°)
0	$0,15$	$0,20$	$-0,15$	$0,41$	$2,91$	$0,62$
10	$10,07$	$0,28$	$9,86$	$0,48$	$13,34$	$0,67$
20	$20,16$	$0,35$	$19,92$	$0,55$	$22,93$	$0,64$
30	$30,02$	$0,30$	$29,97$	$0,20$	$33,49$	$0,37$
40	$40,12$	$0,18$	$39,59$	$0,11$	$44,03$	$0,39$
50	$49,93$	$0,34$	$50,12$	$0,24$	$53,59$	$0,57$
60	$59,87$	$0,22$	$59,76$	$0,33$	$63,50$	$0,45$
70	$70,27$	$0,15$	$70,11$	$0,27$	$74,27$	$0,70$
80	$79,97$	$0,35$	$80,28$	$0,37$	$83,48$	$0,80$
90	$89,87$	$0,30$	$90,07$	$0,41$	$93,52$	$1,04$
100	$100,11$	$0,27$	$100,01$	$0,49$	$103,14$	$1,08$
110	$109,92$	$0,23$	$109,80$	$0,31$	$113,79$	$0,71$
120	$120,22$	$0,21$	$120,11$	$0,15$	$123,48$	$0,87$

Table 2. *Real angle (α) and unperturbed measured angle (average value, α_1, and standard deviation σ_1). Small perturbed measured angle (average value, α_2, and standard deviation, σ_2). Large perturbed measured angle (average value, α_3, and standard deviation, σ_3) .*

Since the effective local curvature has not been measured during trials, we have only a qualitative picture and its maximum range

($0.4\,mm^{-1}$). Anyway, the corresponding error (8°) is never reached in any trial. In order to verify that for small curvature no significative error occurs during shape deformation (groups α_1 and α_2), while a systematic error is not negligible in case of relevant curvatures (group α_3, where relevant curvature can be reached) we have globally considered all the data collected for each trial. In order to obtain a global information on the device behavior, given a certain set of data α_i^j, ($i = 1..3$, $j = 1..5$), where i represents level of perturbation of the curvature and j the particular acquired value, we have computed the samples $\beta_i = \{\alpha - \alpha_i^j,\ j = 1..5\}$. In this way, each of the three samples β_i contains 65 (5 trials for each of the 13 angles in the table) data which represents the absolute errors in evaluating angles by the device with respect to the foreseen ones. In this way, data deriving from measures related to different angles are comparable and a statistic evaluation on the β samples provides a global information on the involved error. The three samples have been analyzed by five two tail Student's t tests, $T_{0,1}, T_{0,2}, T_{0,3}, T_{1,2}, T_{1,3}$. Fixed a significativity level $l = 0.1$, tests $T_{0,i}$ were aimed at proving that sample β_i is draw from a normal population having average value in the theoretical angle value. Tests $T_{0,i}$ were executed to prove that samples β_1 and β_i are draw form the same normal population. First, the following statistics have been computed:

$\bar{\beta}_1$ (°)	σ_{β_1} (°)	$\bar{\beta}_2$ (°)	σ_{β_2} (°)	$\bar{\beta}_3$ (°)	σ_{β_3} (°)
-0.05	0.27	$0,04$	$0,37$	$3,50$	$0,75$

where $\bar{\beta}_i$ is the mean of the sample β_i and σ_{β_i} is its associated standard deviation. In order to verify if β's are sample of a normal population having mean zero the following value for the t test have been computed:

$$
\begin{aligned}
t_{0,1} &= \frac{\bar{\beta}_1 - 0}{\frac{\sigma_{\beta_1}}{\sqrt{65}}} = -1,56 \\
t_{0,2} &= \frac{\bar{\beta}_2 - 0}{\frac{\sigma_{\beta_2}}{\sqrt{65}}} = 0,92 \\
t_{0,3} &= \frac{\bar{\beta}_3 - 0}{\frac{\sigma_{\beta_3}}{\sqrt{65}}} = 37,74
\end{aligned}
\tag{4.27}
$$

Since the two tails t-distribution with 64 degree of freedom which corresponds to a significativity level of 0.1 is equal to 1.67, we can accept the hypotheses that β_1 and β_2 are samples of the supposed distribution. Conversely, since $t_{0,3} > 1.67$ we have to reject the third hypothesis, i.e. *a systematic error is present in the third group of data.* In order to further prove results obtained, two other indicators have been computed:

$$
\begin{aligned}
t_{1,2} &= \frac{\bar{\beta}_1 - \bar{\beta}_2}{\sqrt{\frac{\sigma^2_{\beta_1}}{65} + \frac{\sigma^2_{\beta_2}}{65}}} = -1,65 \\
t_{1,3} &= \frac{\bar{\beta}_1 - \bar{\beta}_3}{\sqrt{\frac{\sigma^2_{\beta_1}}{65} + \frac{\sigma^2_{\beta_3}}{65}}} = -32,85
\end{aligned}
$$

The last two statistics prove that it is possible to suppose (with the same confidence of the previous cases) that β_1 and β_2 are samples draw from the same population, while β_3 have a probability smaller than 1% to be a sample draw from the same normal distribution. Finally, in the following table, p-values related to t-test are reported:

$p_{T_{0,1}}$	$p_{T_{0,2}}$	$p_{T_{0,3}}$	$p_{T_{1,2}}$	$p_{T_{1,3}}$
0.12	0.36	0,00	0.10	0.00

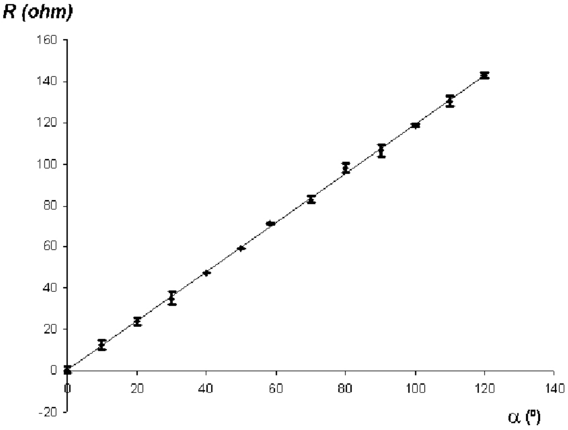

Figure 4.12: *Difference of resistance (and the standard deviation on five trials) between the two layers versus the angle assumed with a light disturbance performed by the stick*

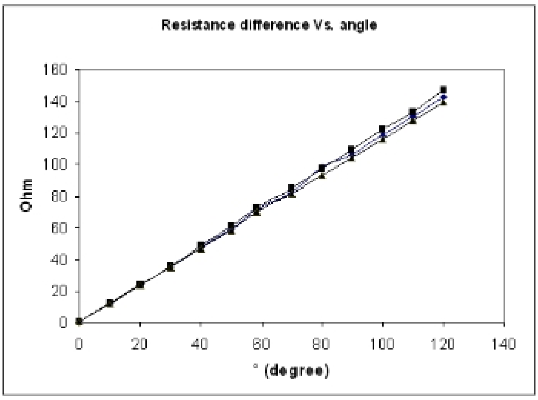

Figure 4.13: *Resistance differences versus the imposed angle under different perturbations.*

4.6 Conclusion and Future Work

In this chapter we discussed the use of textile compatible devices for the measurement of the angle between the initial and final pointing vectors. A sensor of this kind when conformed to a certain object can allow to reconstruct the shape of the object itself. Theory and experiments we have presented confirms that a double layer sensor as described here can act as a wearable electrogoniometer without relevant systematic errors even when the sensor is deformed in a shape having small local curvature (compared with the inverse of the sensor thickness which is of the order of millimeters). This is the situation that can be expected when the sensor is used for gesture capture or other human biometric applications. The integration of this methodology with the same technology employed as length detector, widely explored in previous works, ensures the exact reconstruction of object shapes covered by the double layer sensing fabric, providing concavity and convexity also. We remark that the device is wearable, has very low weight and production cost. For this it seems that it can be used in several application fields, where the posture and gesture analysis is fundamental, as rehabilitation, ergonomics, sport science, virtual and augmented reality. The hypothesis of inextensibility of the substrate supporting the goniometer is removable. However, this case has not been exhaustive treated in this chapter and will be subject-matter of a future work.

4.7 Appendix to this chapter

In the following, the proof of *Lemma* 1 is reported.

Proof. (Sketch) We will see that is possible to construct a curve γ being finite union of circle arcs, such that $\|x-\gamma\|_{C^{2+-}}$ is small as wanted.

Let us divide the interval $[s_1, s_2]$ in n equal subintervals $\{[t_i, t_{i+1}]\}_{i\leq n}$. Let us define the first arc of the approximating curve γ as the unique circle arc having the same initial point, the same initial direction as the curve x and the same final direction at t_2, that is:

$$\begin{cases} \gamma_1(t_1) = x(t_1) \\ \dot{\gamma}_1(t_1) = \dot{x}(t_1) \\ \dot{\gamma}_1(t_2) = \dot{x}(t_2) \end{cases}$$

We remark that in this case the curvature of the chosen arc is equal to the average curvature of x in the interval $[t_1, t_2]$. Since the initial arcs have the same initial condition and and same initial derivative,

$$\|x(t_2) - \gamma(t_2)\| \leq \frac{1}{\sqrt{2}} \sup_{s\in[t_1,t_2]} \left\| \frac{d^2x(s)}{ds^2} \right\| (t_2-t_1)^2.$$

Let us now construct n arcs by attaching a new arc to the previous one in a way that the direction always follows the curve x at junction points. More precisely, the arcs are inductively defined by the following relation

$$\begin{cases} \gamma_{i+1}(t_i) = \gamma_i(t_i) \\ \dot{\gamma}_{i+1}(t_i) = \dot{x}(t_i) \\ \dot{\gamma}_{i+1}(t_{i+1}) = \dot{x}(t_{i+1}) \end{cases}$$

in this case, we obtain:

$$\sup_{s\in[s_1,s_2]} \|x(s) - \gamma(s)\| \leq \frac{1}{\sqrt{2}} \sum_{i=1}^{n} \sup_{s\in[s_1,s_2]} \left\| \frac{d^2x(s)}{ds^2} \right\| (t_{i+1}-t_i)^2. \quad (4.28)$$

The right hand side of inequality 4.28 is bounded by $\leq \frac{\|x\|_{C^2}}{n}$, which decreases to 0 when n increases. Moreover, about directions we have

$$\sup_{s\in[s_1,s_2]} \|\dot{x}(s)-\dot{\gamma}(s)\| \leq \sup_{s\in[s_1,s_2]} \left\|\frac{d^2x(s)}{ds^2}\right\| \frac{s_2-s_1}{n}.$$

Finally, since the curvature $\ddot{x}$ is uniformly continuous and at each arc the curvature of the arc is equal to the average curvature of the corresponding interval of x then it holds

$$\sup_{s\in(t_i,t_{i+1})} \|\ddot{x}(s)-\ddot{\gamma}(s)\| \to 0$$

as $n \to \infty$ on each interval. By considering left and right second derivative we can include in a similar way the endpoints $\{t_i\}_{i\leq n}$ estimating the distance between the two curves and the respective first and second derivatives, which constitutes the C^{2+-} norm. By this the statement is proved. ■

Chapter 5

Low Skin Motion Artifact SCEEG for Lumbar Spine Monitorization

5.1 Introduction

Textile based piezoresistive transducers are an innovative category of devices that use yarns made of conductive and elastic fibers or screen printed conductive rubber coatings to sense strain. They usually satisfy wearability requirements and are used in real-time information gathering systems, being comfortable, ubiquitous and available for long term monitoring. They include knitted fiber transducers (KFTs), sewed fiber transducers (SFTs) and smeared redundant elastomer (SRETs) transducers [18].

In the latter category, SRETs constituted by Conductive Elastomers (CEs) have been currently employed as strain sensors networks to detect human posture and gesture. Elastic interconnection wiring is also easily realized leading to monolithic fabrication techniques which avoid the presence of metal wires and multiple solderings. Despite this, there is a strong dependence of the system performance by the body structure garment fitting. Moreover, the non-linear dynamical behaviour of SRETs requires identification algorithms, functions which relate joint angles to electrical values presented by the sensor network. The construction of these functions is quite complex and time of computation dramatically increases with the number of degrees of freedom and with the accuracy required to the system to be resolved [12].

Recent development of CEs sensor modeling overcomed some of their main limitations and introduced new fields of operability in SRETs networks. In particular, in strain applications, we introduced in Chap. 3 a useful data processing technique for treating the non-linear dynamical response, considering the different behaviour in sensor elongation and relaxation: actually, when the sensor in stretched, the internal cross-links of the polymeric chains tend to break producing the breakdown of cabon black agglomerates and an increase in resistance. Inversely, when the sensor is relaxed, the cross-link readjustment leads to different electrically conductive paths in respect to the previous states. This technique needs an implementation in multisensory systems, but leads to encouraging results in biomechanical reconstruction.

Furthermore, in Chap. 4, we introduced a novel approach in CEs sensing, relating the global curvature of a layer to its electrical resistance value variation and exploring under which condition the resistance can be considered uncorrelated with its particular local bending profile. These devices are called Smeared Conductive Elastomer Electrogoniometers (SCEEGs) and under particular configuration they can be employed as on-body electrogoniometers (Sec. 5.2.2). The integration of SRET arrays and SCEEGs is definitely a powerful tool for human body posture and gesture reconstruction through efficient and fast algorithms.

In this paper we intrduce a particular realization of CE strain sensors deposed on an adhesive taping, obtaining a very low skin artifact device (VLSA). Moreover we present an electrogoniometric system in which the inextensible insulating layer of Chap. 4 has been replaced by an elastic layer, allowing the system to be employed both as strain sensor and as electrogoniometer. Finally, we present a biomechanical application in lumbar spine posture monitorization. As a matter of fact, it is known from literature that in the sagittal balance there is a strong correlation with the torso angle and geometrical parameters of lumbar vertebraes, such as the angle between subsequent upper endplates ([10], [11]) Data obtained from piezoresistive sensors are so suitable to be used in biomechanical analysis in order to predict forces and moments acting on the functional units of the lumbar spine.

5.2 Materials and Methods

CE we used is a commercial product by WACKER Ltd (Elastosil LR 3162 A/B) and it consists of a mixture containing graphite and silicone rubber. WACKER Ltd guarantees the non-toxicity of the product that, after vulcanisation, can be employed in medical and pharmaceutical applications [12].

5.2.1 Low Skin Artifact CE sensor

CEs are commonly used deposed on an elastic textile substrate, such as *Lycra*, for the realization of the so-called *smart garments.* It is known that major errors committed in these sensorized garments rely on artifacts due to the relative motion between skin and tissue and to creases that occur when the textile substrate is uderstretched.

In order to overcome the aforementiond issues, we spreaded CEs directly onto a commercially available *Kinesio* tape ([19]) realized in an elastic woven cotton with a substrate of medical grade heat sensitive acrylic adhesive for skin contact ([20]). The fabricant declares elasticity of up to 40% from resting length.

An example of such system is presented in Fig. 5.1(a), 5.1(b),5.1(c) and 5.1(d), where a single strip of CE has been spreaded on a portion of tape and adapted on the wrist. The obtained sensor is highly adherent to skin in the joint ROM and can be used as long as the tape is designed to be used, without presenting comfort or obtrusivity issues. Furthermore, the electrical response of CE is not altered by the particular substrate, the textile guaranteeing insulation between skin and sensor.

5.2.2 Carbon Elastomers as Elastic Electrogoniometers

According to Chap. 4, two alternative configurations are available for the realization of an SCEEG sensor: single and double-layer.

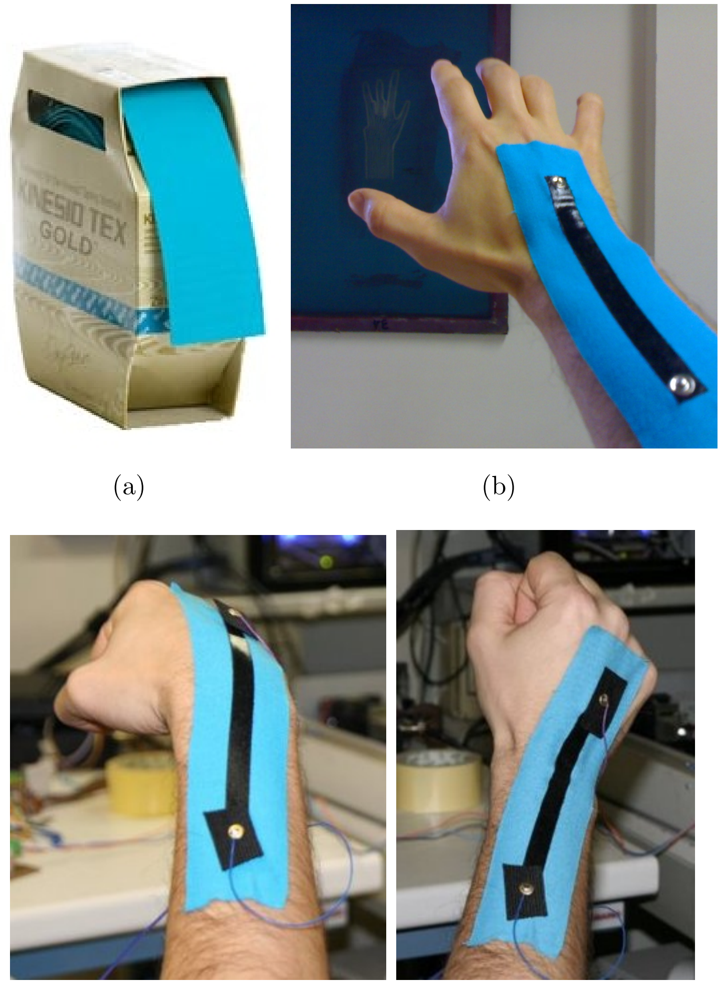

(a) (b)

(c) (d)

Figure 5.1: (a)A roll of *Kinesio* tape; (b) A VLSA CE specimen applied on the wrist; (c) Sensor adherence on wist flexion and on (d) wrist extension.

Since with a single-layer sensor we cannot set elongation effects apart from bending effects, it is necessary to adopt a double-layer configuration: in this way elongation effects cancel themself out and the angle can be valued by the difference of resistance

$$\Delta R = \Delta R^A - \Delta R^B$$

obtained by subtracting the resistance value of the upper layer A from the resistance of the lower layer B.

Indeed, it was found that for small deformations and with an inextensible insulating layer, the relation between the global curvature of the sensor and its electrical resistance is linearly related with its resistivity ρ by the following:

$$\Delta R \simeq 2\rho\Delta\alpha \tag{5.1}$$

where a single layer is modeled as a sequence of curves made of circular crowns (Fig. 4.3). Recalling geometrical properties of regular planar curves $\Delta\alpha$ is defined as:

$$\Delta\alpha = \int_{s_0}^{s} k(s)\ ds$$

in which $k(s)$ is defined as the curvature of a C^2 parametrized curve in normal form $x(s)$, and s is its arc length.

Furthermore, in a double-layer configuration, the theoretical error committed by the approximation in Eq. 5.1 is less than 4% in the range of curvatures measured in the aforementioned study.

5.3 Device Fabrication and Experimental Setup

5.3.1 Specimen Realization

Aiming at the design of an extensible smeared carbon elastomer electrogoniometer, able to gather information on the surface curvature of a bending human joint, particular attention has been paid at minimising the sensor stiffness in order to preserve the joint functional ability and the normal skin deformation. Moreover, in order to avoid inaccuracies due to the manual deposition processes, CE layers have been realized by milling a single Teflon mould as reported in Fig. 5.2 with relative dimensions. Subsequently, the two layers have been superimposed and insulated by the same elastic substrate of Sec. 5.2.1 as in Fig. 5.3 and connected by wire to the electronic hardware of Sec. 5.3.2.

5.3.2 Data Acquisition and Processing

In order to measure sensor resistance an ad-hoc analog electronic front-end has been realized and the schema is reported in Fig. 5.4. Needing to made electrical contacts on CE film itself, Kelvin (four-point probes) resistance measurement method is suitable to neglect contacts and wire resistances. The costant current generator and the instrumental amplifiers for the voltage measurement is implemented on the same single electronic board. The costant current generator has been made by an LM324AN operational amplifier in Howland configuration. AD620 instrumental amplifier are used to measure

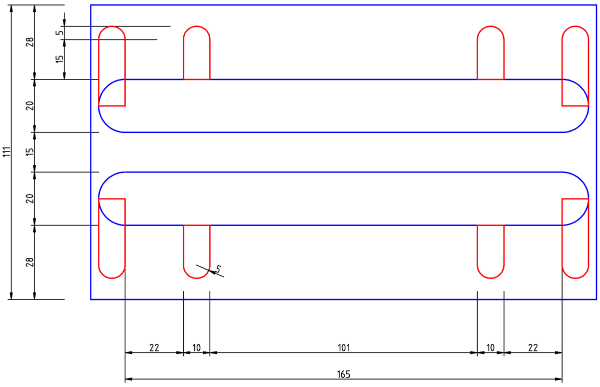

Figure 5.2: Design schema and dimensions of the Teflon mould with a couple of sensors for the milling machine. The blue sector is the main part of the sensor, whereas red sectors indentify the connection points to wires of the data acquisition device. Thickness of the mould: $0.45mm$.

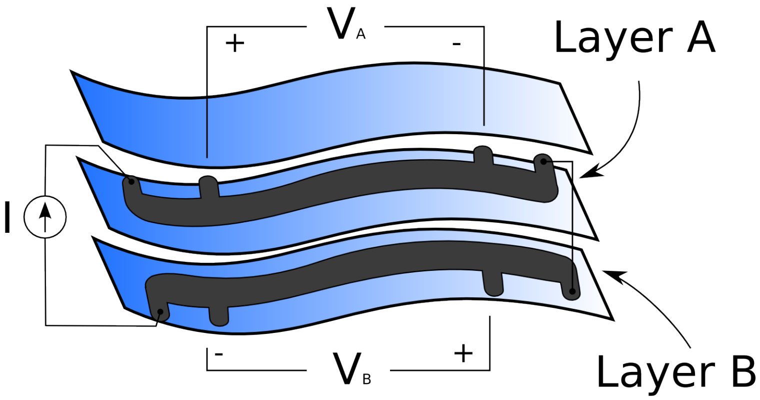

Figure 5.3: Double layer schema and electric notation: the two sensors are insulated by stripes of the elastic adhesive *Kinesio* tape.

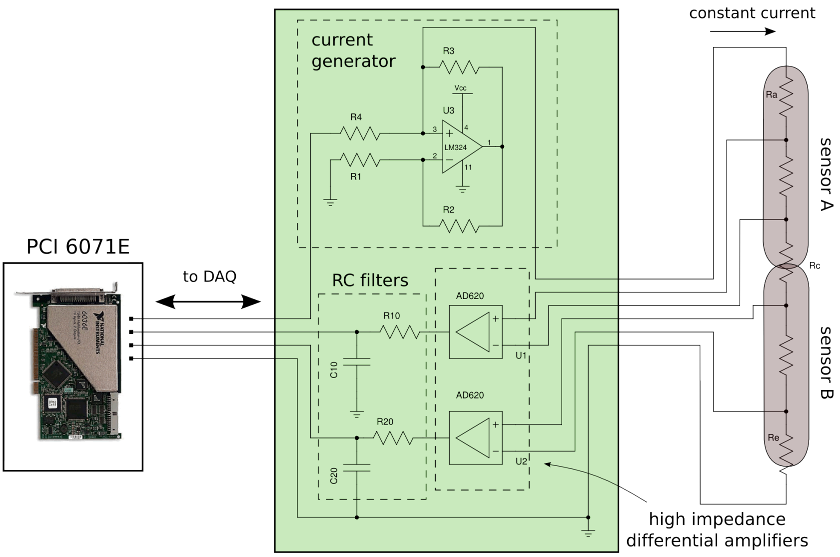

Figure 5.4: Analog Devices Interface: a constant current is generated and issued in the two sensors, while the voltage drop is read by high impedance amplifiers realizing the four-point contact method.

voltage drop across the CE sensors: the high input impedance stage grants no voltage drop on contacts and connection wires. Adjustable AD620 gain has been set to be unitary.

Data acquisition has been performed by the PCI-6071E multifunction DAQ by National Instruments. In order to adjust the current issued into the sensors, the Howland current source has been controlled by the DAQ hardware analog output.

5.3.3 SCEEG Characterization

The mechano-electrical behaviour of a CE sensor is given as relations between its electrical resistance and the strain applied to the sensor itself. We calculate its resistivity as:

$$\rho = R\frac{A}{l} \tag{5.2}$$

where R is the electrical resistance, A is the cross-sectional area and l the length of the specimen. We measured the resistance by the four-point contact method ([21]) supplying a single piezoresistive film with costant currents up to 301±1 μA, under elongations up to 250%. Obviously, the behaviour in compression is not contemplated and values are considered to be consistent only from the resting values R_0,l_0. The resistance and the resistivity present the behaviours of Fig. 5.5(a) and 5.5(b) relatively.

In the field of low strains, up to 20%, the resistance can be well approximated by a linear regression: indeed for the double layer system, both correlation coefficients are $R^2 = 0.98$ and regression values are resumed in Table 5.1. Considering the specimen isovolumic during deformation (dimensions on Fig. 5.2), and $R(l) = ml+q$, the resistivity cannot be considered constant and its value is given substituting $R(l)$ in Eq. (5.2):

$$\rho(l) = \frac{mV_0}{l} + \frac{qV_0}{l^2} \tag{5.3}$$

Calibration hardware and results are reported in Fig. 5.6(a), 5.6(b) and 5.6(c).

The manual spreading process and assembly of CEs inevitably leads to intrinsic different electrical properties of specimens. Since

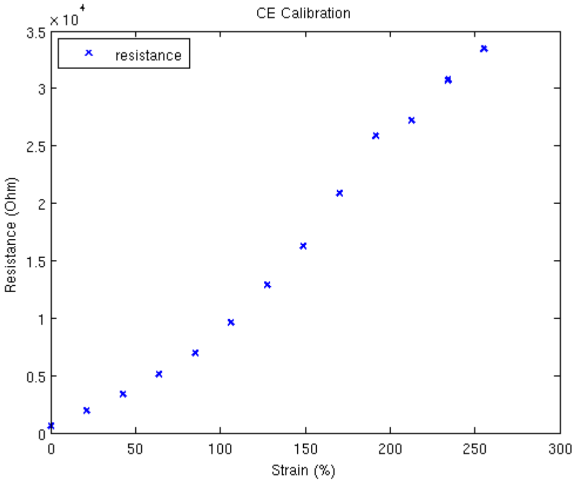

(a)

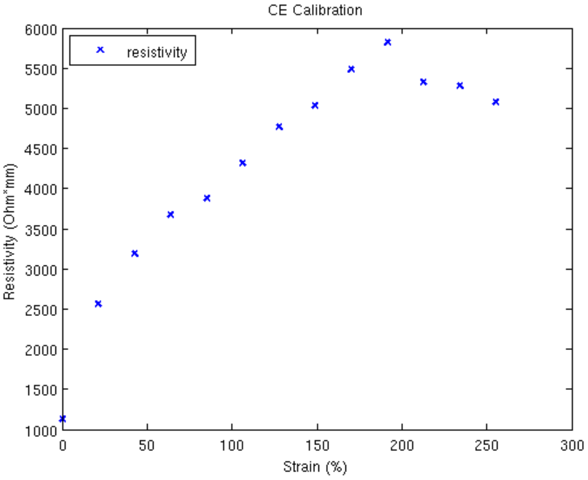

(b)

Figure 5.5: Effect of large uniaxial strain on (a) the electrical resistance and on (b) the resistivity of a previously unstrained CE specimen.

we can't control the resistance value during the double layer superimposition, a calibration step is needed in order to determine the sensors gauge factor ($GF = \frac{\Delta R L_0}{\Delta L R_0}$) and to correct sensor reading, so that they provide the same output during uniaxial deformation (as explained in Sec. 5.2.2).

Referring to the couple of sensors as A and B, they exhibited a GF of 11.92 and 11.90 respectively. Indicating with $y_B = m_B x + q_B$ the electrical output of sensor B, we consequently correct this latter value by the following relation:

$$\hat{y}_b = \frac{m_A}{m_B} \cdot y_b - \frac{m_A}{m_B} \cdot q_B + q_A \tag{5.4}$$

$$\hat{y}_b = m^* y_b + q^* \tag{5.5}$$

that necessarily leads to $\hat{y}_b = m_A x + q_A = y_A$. We assumed by calibration values that the error committed in the correction of Eq.5.4 is less than 2%.

Finally, the same strategy can be obtained, defining a relative calibration between sensors, finding the fit of sensor A resistance in respect to sensor B: assuming that resistance are linear function, this procedure consist in a change of reference frame, leading to the same angular coefficient of Eq. 5.5, but with a different offset. This latter procedure doesn't need any particular calibration hardware except that the sensors need to be elongated uniaxially (Fig. 5.7).

5.4 Experimental Results and Discussion

Once the double layer system is calibrated as in Sec. 5.3.3, both resistances hold the same value during uniaxial elongation. Subsequently, if the system is bended as in Fig. 5.8(a) and 5.8(b), we

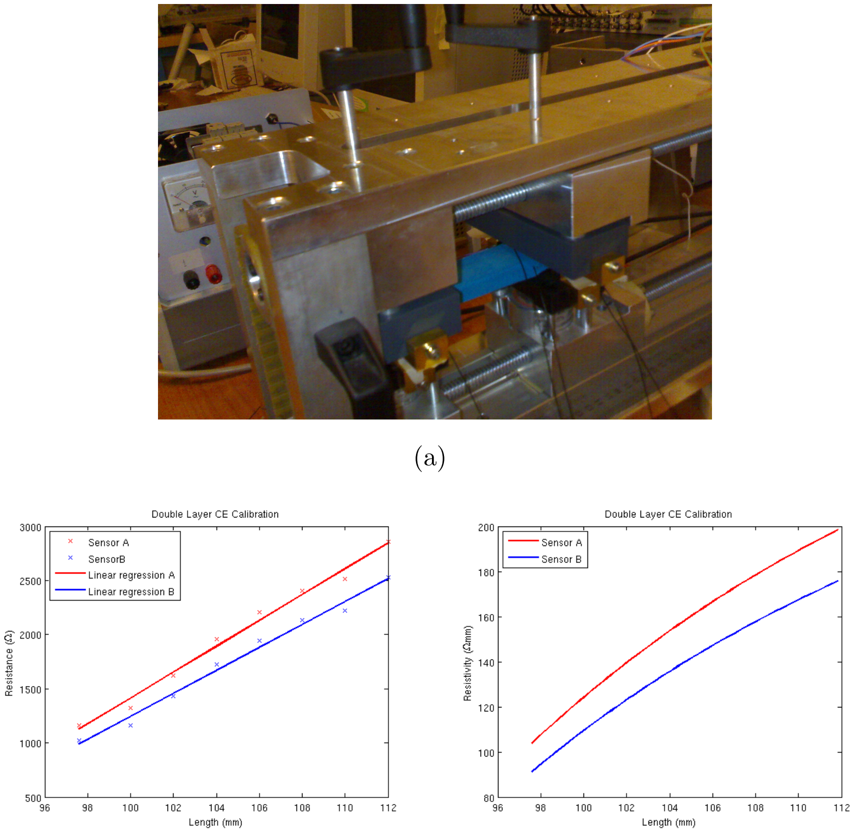

(a)

(b)

(c)

Figure 5.6: (a) Calibration session of the Double Layer system on dedicated hardware (courtesy of *Smartex*, Italy); (b) Linear regressions on resistance values ($R^2 = 0,98$); (c) Resistivity trend from Eq. 5.3.

Table 5.1: Linear regressions of calibration curves for sensors A and B relating resistance to length. Equations in the form $R = m \cdot l + q$.

Sensor	m $[\Omega/mm]$	q $[\Omega]$
A	119.39	-10526.05
B	106.14	-9369.60

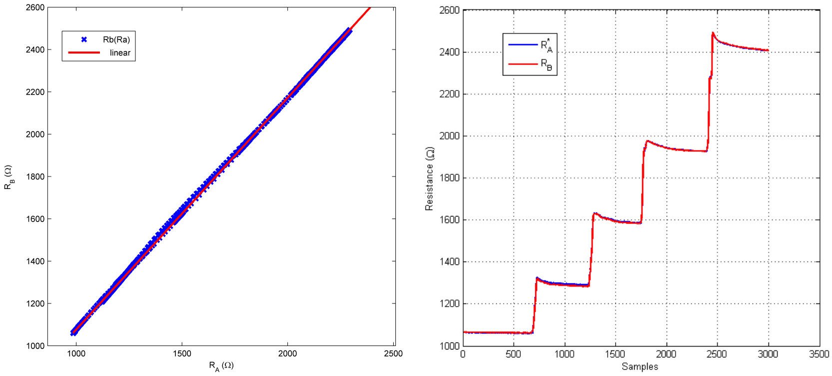

(a) (b)

Figure 5.7: Relative fast-calibration procedure.

expect to find a linear relation between the global curvature and the resistance differences, as of Eq. 5.1, according with Chap. 4.

5.4.1 Slab Bending

A series of trials were performed, extending and bending arbitrarily the double layer system on an aluminium slab. During these trials, the external reference angle was measured by a couple of SG150 electrogoniometers (Biometrics Ltd), whose extensions were directly attached on the aluminium clamps (Fig. 5.8(a)). Data from electrogoniometers and from CEs were synchronised by a reference signal directly given by the DAQ of Sec. 5.3.2. Only positive elongations are accounted in this report, because the procedure of Chap. 3 will be implemented only after the assessment of this technique.

Observing the trends of Fig. 5.8(c) we can appreciate the accuracy of the system during one of these series of trials, where CE data processed are compared to the electrogoniometer output. The system accuracy is strong with a maximum error of 3.4 degrees and a RMS error of 1.34 degrees.

5.4.2 Sensor Perturbations

In these trials a shape perturbation has been imposed to the system: the central part of the sensor has been deformed by the insertion of three cylindrical elements, as in Fig. 5.9(a). Dimensions are reported in Fig. 5.9(b).

The output of the sensor reading in reported in Fig. 5.9(c). Knowing the geometry from Fig. 5.9(b), we expect to read an angle that is $2\gamma \simeq 2 \cdot tan^{-1}(\frac{d}{2a}) = 10.16$ degrees. The sensors output after 30 sec is 10.36 degrees, with an error of 1.9%.

5.4.3 Spine Monitorization

Finally, a series of trials has been performed positioning the SCEEG sensor on the spine of a volunteer, asking him to perform normal movement of flexion-extension of his spine.

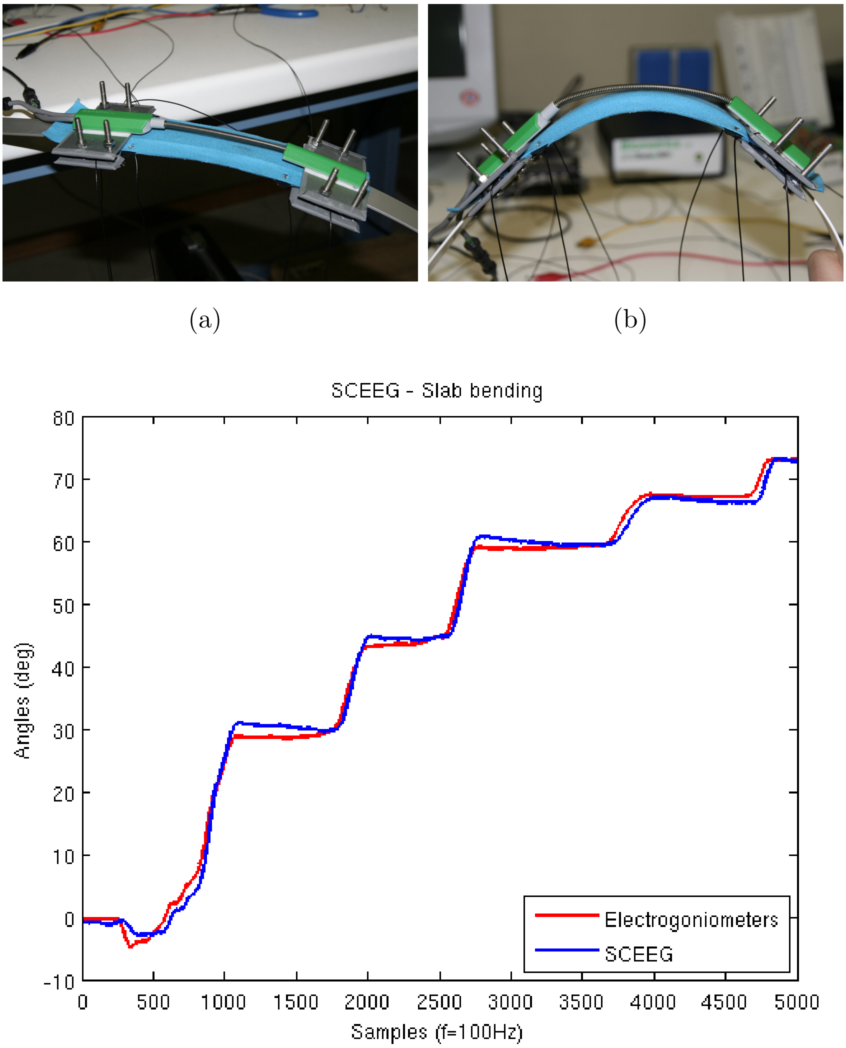

(a)

(b)

(c)

Figure 5.8: (a) Experimental setup: the double layer system is layed on an aluminium slab acting as guide, whereas electrogoniometers are placed upon the clamps; (b) Imposed deflexion; (c) Output comparison of a series of trials for angles between 0 and 70 deg.

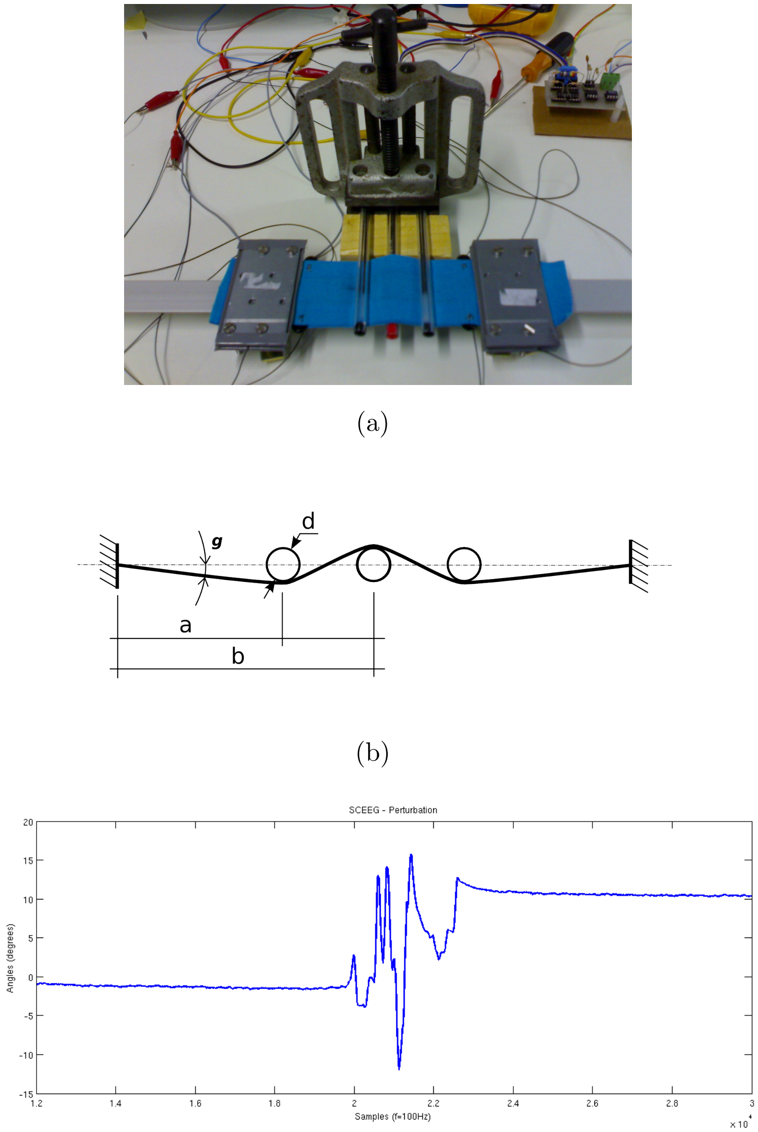

(a)

(b)

(c)

Figure 5.9: (a) Imposed perturbation on the central part of the sensor; (b) Schematic drawing with quotes: $a = 45mm$, $b = 60mm$, $d = 8mm$; (c) Sensor trend before, during and after the perturbation.

The sensor has been layed in proximity of the lumbar portion of the spine, slightly displaced on the right side of the central axis, in order to place a normal single-sensor strip in the left side (Fig. 5.10(a)). This latter sensor was used to monitorize creases reduction using the *Kinesio* textile in respect to *Lycra*.

The volunteer was asked to perform sessions of flexion-extension, spacing out the flexion movements in three separate steps, whereas extension has been performed in a continuous movement.

Results of one of these trials are summarised in Fig. 5.10(b) and 5.10(c). The SCEEG sensor was previously calibrated using data from Sec. 5.4.2 and Fig. 5.10(b) shows the voltage difference plotted in respect to the angle obtained with *Biometrics* electrogoniometers: a higher dispersion is observable in the plot in respect to those obtained in trials of Sec. 5.4.1 and 5.4.2. Reasons are mainly due to the inaccuracy of the sensor position on the skin, that leads to a difficulty of performing an on-body calibration. Despite this, the SCEEG sensor shows the expected behaviour, except for the relaxation part, not treated for reasons explained in Sec. 5.3.3.

In conclusion, this work demonstrated that the use of CE sensors for electrogoniometry applications in biomechanics lead to strongly profitable results. Their implementation in low skin artifacts system are the way to reduce errors commonly committed in normal textile applications. Finally, their coupling with strain computation and in multisensory networks, will definitely provide a more accurate long-term and comfortable monitorization of biomechanical variables.

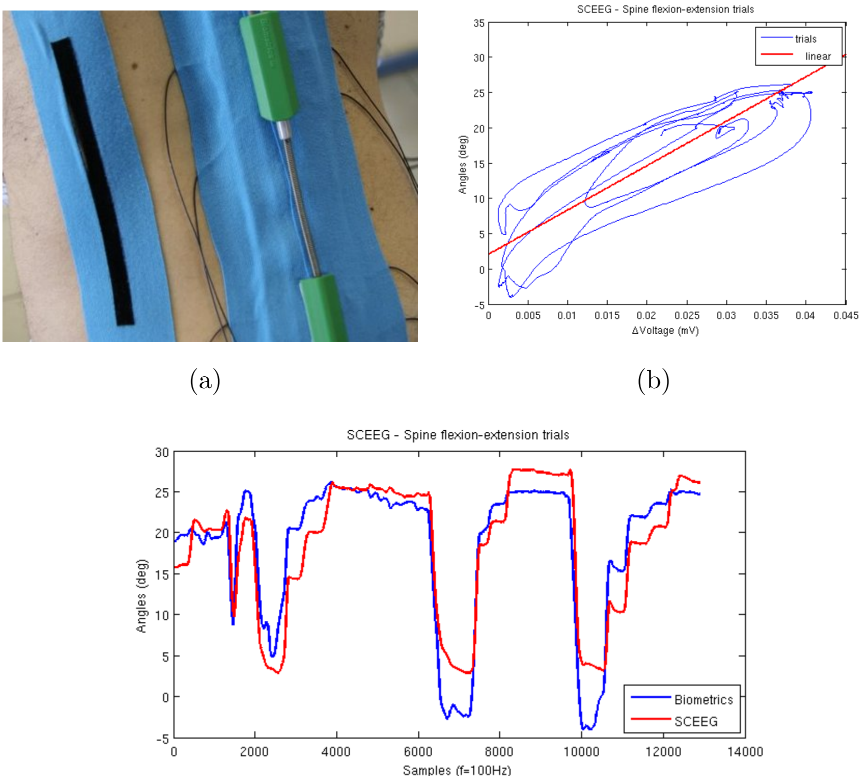

(a) (b)

(c)

Figure 5.10: (a) Positioning of the VLSA sensor and the SCEEG sensor on the lumbar spine; (b) Linear regression of SCEEg sensor; (c) SCEEG output during flexion-extension movements.

Bibliography

[1] Burton K Adams M, Bogduk N and Dolan P. *The biomechanics of back pain - 2nd edition.* Churchill Livingstone, 2006.

[2] R. Op De Beeck and V. Hermans. Research on work-related low back disorders. *Institute for Occupational Safety and Health - European Agency for Safety and Health at Work*, 2000.

[3] BP Bernard. Musculoskeletal disorders (msds) and workplace factors: a critical review of epidemiologic evidence for work-related musculoskeletal disorders of the neck, upper extremity, and low back. *US Department of Health and Human Services, National Institute of Occupational Safety and Health USA*, 1997.

[4] G Calvosa and Dubois G. *Rehabilitation in the Dynamic Stabilization of the Lumbosacral Spine.* Springer, 2008.

[5] Morris J.M. Nachemson A. In vivo measurements of intradiscal pressure: discometry. a method for the determination of pressure in the lower lumbar discs. *Journal of Bone Joint Surgery*, 1964.

[6] Zanetti M et al. Pfirrmann CS, Metzdorf A. Magnetic resonance classification of lumbar intervertebral disc degeneration. *Spine*, 2001 Sep 1;26(17):1873-8.

[7] N. Campbell-Kyureghyan, M. Jorgensen, D. Burr, and W. Marras. The prediction of lumbar spine geometry: method development and validation. *Clinical Biomechanics*, 20(5):455–464, 2005.

[8] Kapandji IA. *Physiologie articulaire. Tome 3: tronc et rachis.* Maloine 1982, 1982.

[9] F. D Osualdo, S. Schierano, and C. Cisotti. The evaluation of the spine through the surface. The role of surface measurements in the evaluation and treatment of spine diseases in young patients. *EUROPA MEDICOPHYSICA*, 38(3):147–152, 2002.

[10] MA Adams, P. Dolan, C. Marx, and WC Hutton. An electronic inclinometer technique for measuring lumbar curvature. *Clin Biomech*, 1(3), 1986.

[11] P.M.M. Saur, F.B.M. Ensink, K. Frese, D. Seeger, and J. Hildebrandt. Lumbar Range of Motion: Reliability and Validity of the Inclinometer Technique in the Clinical Measurement of Trunk Flexibility. *Spine*, 21(11):1332, 1996.

[12] A Tognetti, F Lorussi, R Bartalesi, S Quaglini, M Tesconi, G Zupone, and D De Rossi. Wearable kinesthetic system for capturing and classifying upper limb gesture in post-stroke rehabilitation. *Journal of NeuroEngineering and Rehabilitation*, 2(8), March 2005.

[13] Luinge H.J. *Inertial Sensing of Human Movement.* Twente University Press, 2002.

[14] Tesconi M. *A Wearable System for Lower Limb Movement Analysis.* PhD Thesis - University of Pisa, Italy, 2007.

[15] U. Holmberg, P. Myszkorowski, Y. Piguet, and R. Longchamp. On compensation of nonminimum-phase zeros. *Automatica(Oxford)*, 31(10):1433–1441, 1995.

[16] J. J. Reilly D. M. Sherrill, M.L Moy and P. Bonato. Using hierarchical clustering methods to classify motor activities of copd patients from wearable sensor data. *Journal of NeuroEngineering and Rehabilitation 2005*, 2(16), 2005.

[17] A.L. Schawlow D.A. Kleinman. Corbino disk. *Journal of Applied Phys.Vol 31, 2176*, 1960.

[18] E.P. Scilingo A. Tognetti F. Lorussi, W. Rocchia and D. De Rossi. Wearable redundant fabric-based sensors arrays for reconstruction of body segment posture. *IEEE Sensors Journal*, 4(6):807–818, 2004.

[19] Kinesio UK. A Brief History of Kinesio Tex Taping. *http://www.kinesiotaping.co.uk/history.jsp.*

[20] JF Kenney, TH Haddock, RL Sun, and HC Parreira. Medical-grade acrylic adhesives for skin contact. *Journal of applied polymer science*, 45(2):355–361, 1992.

[21] K. Yamaguchi, JJC Busfield, and AG Thomas. Electrical and mechanical behavior of filled elastomers. I. The effect of

strain. *Journal of Polymer Science Part B Polymer Physics*, 41(17):2079–2089, 2003.

Acknoledgements

The author wants to sincerely thank Prof. Danilo De Rossi for the research opportunity and Dr. Federico Lorussi for his scientific contribution to this work. In addition, author is obliged to Simone Bracaloni and to the research group at the Biomechlab laboratory in Navacchio for their technical contribution.